MILLENNIAL-SCALE VARIABILITY IN THE INDIAN MONSOON AND LINKS TO

OCEAN CIRCULATION

By

KIMBERLY DELONG

BS Environmental Geology, University of North Carolina – Chapel Hill, 2008

THESIS

Submitted to the University of New Hampshire

in Partial Fulfillment of

the Requirements for the Degree of

Master of Science

in

Oceanography

May, 2015

This thesis has been examined and approved in partial fulfillment of the requirements for the degree of Master of Science in Oceanography by:

Thesis Director, Dr. Rosemarie E. Came, Assistant Professor of Climate Science

Dr. Joel E. Johnson, Associate Professor of Geology

Dr. Liviu Giosan, Associate Scientist with Tenure

Woods Hole Oceanographic Institution

On October 22, 2014

Original approval signatures are on file with the University of New Hampshire Graduate School.

To hold eternity in an hour

And infinity in the palm of your hand,

To see a heaven in a wild flower

And a world in a grain of sand.

- William Blake,

arr. by K. deLong

Acknowledgements

Table of Contents

Abstract

MILLENNIAL-SCALE VARIABILITY IN THE INDIAN MONSOON AND LINKS TO

OCEAN CIRCULATION

By

Kimberly DeLong

University of New Hampshire, May, 2015

Millennial-scale variability in the Indian monsoon was temporally linked to changes in global ocean circulation during the last glacial period, as evidenced by planktic-benthic foraminiferal stable isotope and trace element results from an intermediate depth sediment core from the northwestern Bay of Bengal (Core NGHP-01-19B; 18°58'N, 85°39'E; 1,422 m). Paired planktic foraminiferal Mg/Ca and $\delta^{18}O_c$ of *G. ruber* constrain sea surface temperatures and isolate millennial-scale variations in the $\delta^{18}O$ of surface waters ($\delta^{18}O_{sw}$) which resulted from changes in river runoff in the northwestern Bay. Concurrently with low $\delta^{18}O_{sw}$ events, benthic foraminiferal $\delta^{13}C$ of *Cibicidoides* spp. decreased, suggesting an increased influence of an aged water mass at this intermediate depth site during the low salinity events. Benthic foraminiferal Cd/Ca of *H. elegans* supports the identification of this water mass as aged Glacial Antarctic Intermediate Water (GAAIW). Lagged correlation analysis (r= 0.41) indicates that changes in subsurface properties led changes in surface properties by an average of 380 years. The implication is that Southern Hemisphere climate exerted a controlling influence on the Indian monsoon during the last glacial period.

Introduction

The most densely populated region of the world also happens to be the region affected by the Earth's largest monsoon system. The livelihoods and cultures of over three billion people are dependent on the annual summer downpour known as the Asian monsoon (Figure 1). Historically, changes in the intensity of the Asian monsoon have caused both floods and droughts, devastating large areas and often leading to crop ruination and famine (Cook et al., 2010). Despite its vast influence, little is understood about what controls the timing and intensity of the Asian monsoon. Predictions of rainfall in climate models are still unreliable, despite considerable research effort aimed at constraining rainfall over land, one of the most essential aspects of climate to daily life (Malik et al., 2012). As atmospheric CO_2 concentrations increase, the climate system is expected to respond; but there exists little paleoclimate data upon which to base predictions of the response of the monsoon during periods of rapid climate change.

The Asian monsoon can be divided into two geographic subsystems, the East Asian monsoon and the Indian monsoon, which both operate in a similar way but may or may not be connected to the same forcing mechanisms (Johnson, 2011). The basic meteorological forcing for the Indian monsoon is the seasonal difference in temperature between the land and sea, which drives a biannual reversal of the continent-wide wind patterns. During the winter, or northeast monsoon regime, the main winds in the northern tropics blow away from India and towards the southwest. In summer, the heating of the Eurasian land mass creates a pressure difference between the continent and the ocean. An intensely low atmospheric pressure system hovers over the Tibetan Plateau from June to September, driving cross-equatorial winds and dumping torrential rains onto the Indian sub-continent, creating the summer, or southwest, monsoon.
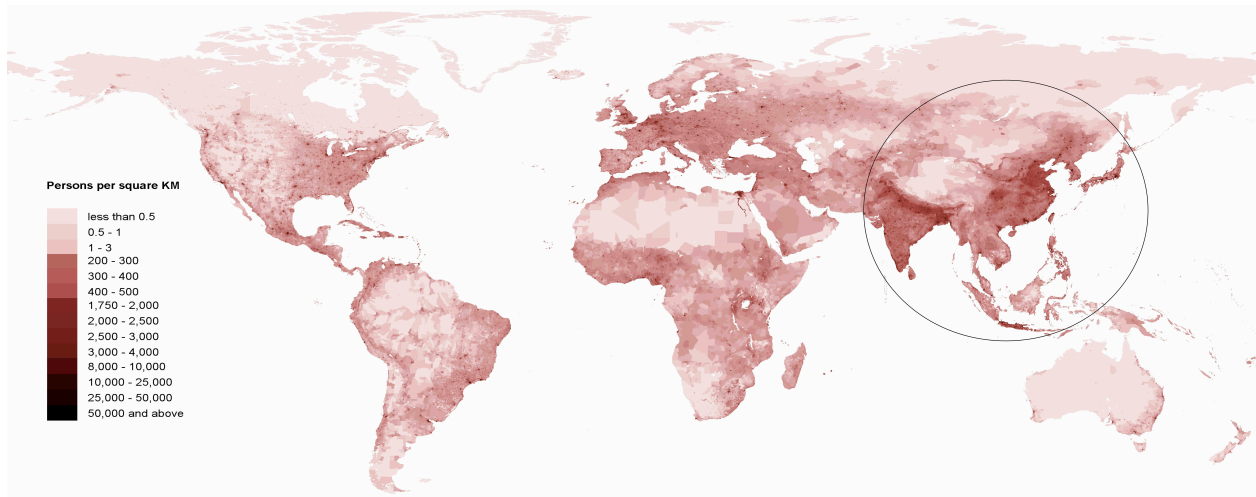
Figure 1. Earth's Population. More people live inside this circle than outside of it (Dewey 2013). This is not only the earth's most populated region, but also includes the area affected by the Asian monsoon.

Orbital Timescales

Since the direct cause of monsoons is solar heating, Asian monsoon variability on geologic time scales is believed to respond to Milankovich orbital forcing (e.g., Prell and Kutzbach 1987; Clemens et al 1991; Ziegler et al 2010). Milankovich theory states that insolation varies predictably at periodicities of 23, 41, and 100 thousand years due to changes in Earth's orbital parameters (Croll, 1864; Milankovich, 1941). The parameter that most strongly affects insolation at the tropics, where the monsoon system is located, is precession (the direction of the Earth's tilt). Models suggest that monsoon intensity should be at zero-phase with precession minima (insolation maxima) (Ruddiman, 2006). However, this forcing is not clear in climate records (Caley et al., 2011). Furthermore, as with many climate signals, records of monsoon intensity are dominated by suborbital scale variability (e.g., Wang et al., 2001), also known as millennial scale climate events, the causes of which are poorly understood.

Many proxies for Indian monsoon strength have been considered in order to test the hypothesis that orbital-scale changes in summer insolation impact the intensity of the monsoon. For historical and political reasons, the Bay of Bengal has not always been accessible for direct sampling. As such, records of wind intensity or upwelling in the Arabian Sea are more prevalent (Caley et al., 2011; Clemens and Prell, 2003; Ziegler et al., 2010). Since monsoons are driven by pressure differentials, intensity of rainfall is expected to tightly correlate to records of wind strength. However this assertion is yet to be directly supported (Bolton et al., 2013); and it has been suggested that there can be a decoupling between wind strength and precipitation in the Indian monsoon related to the position of the ITCZ (Malaizé et al., 2006).

One major study examining five proxies from the Arabian Sea found that the peak in monsoon intensity (as measured in records of upwelling) contained a roughly equal amount of

variance at the precession (23 k) and obliquity (41 k) frequencies (Clemens and Prell, 2003). The obliquity frequency was in-phase to NH summer insolation maxima, but at the precession frequency there was a lag of 7.7 ± 0.9 k.y.a., or 121° ± 14° (Clemens and Prell, 2003). Since this phase lag is greater than 90° (more than a quarter of the 23 kyr cycle), the precession forcing of the Indian monsoon system is concluded to be non-linear (Bolton et al., 2013; Clemens and Prell, 2007, 2003). Suggested forcing mechanisms internal to the climate system include changes in the pressure gradient between Asia and the Southern Indian Ocean (Bolton et al., 2013).

Although this ~8 kyr lag was not expected from the zero-phase orbital hypothesis, other studies corroborate the finding. Accumulations of marine organic carbon in the Arabian Sea indicate a lag of about 7000 years at the precession frequency (Ziegler et al., 2010). Additionally, the difference in $\delta^{18}O$ between surface-dwelling and thermocline-dwelling foraminifera in the equatorial Indian Ocean suggests that monsoon strength (least stratification) lagged precession insolation forcing by 9 kyr (Bolton et al., 2013). Farther afield, pollen records east of Japan suggest that the East Asian monsoon also lagged precession insolation maxima by about 8 kyr (Morley and Heusser, 1997). These studies lend support to the Clemens and Prell (2003) result. However, the conclusion that this lag is representative of monsoon intensity is not unanimously agreed upon by the paleoclimate community (e.g., Ruddiman, 2006).

As most of the Arabian Sea reconstructions record variations in upwelling or productivity, one criticism is that they may be influenced by winter winds as well as summer monsoon winds (Ruddiman, 2006). It has also been suggested that productivity in the Arabian Sea was decoupled from monsoon intensity at the precession frequency (Ziegler et al., 2010). Indeed, modeling studies suggest that productivity and the intensity of the oxygen minimum zone (which affects denitrification and carbon preservation) are highly sensitive to global ocean

circulation (Schmittner et al., 2007) rather than to changes in monsoon-driven upwelling. Furthermore, many speleothem records, which measure precipitation via oxygen isotopes, indicate a strongly synchronous relationship between orbital insolation forcing and monsoon intensity (Ruddiman, 2006; Wang et al., 2001). Thus, the relationship between the Indian monsoon and the precession frequency of insolation is still unresolved.

Millennial Timescales

Superimposed on orbital scale variability are shorter climate fluctuations known as millennial scale events (Figure 2; Blunier and Brook, 2001). These events were first found in the $\delta^{18}O$ of glacial ice from Greenland ice cores (GRIP and GISP2) (Greenland Ice-core Project (GRIP) Members, 1993; Grootes et al., 1993), as well as in benthic foraminiferal records from the North Atlantic (e.g, Bond et al., 1993). The previously long-held paradigm was that climate perturbations originate in the high-latitude North Atlantic and propagate globally via changes in the flux of North Atlantic Deep Water (NADW) (e.g. Weyl 1968; Broecker et al., 1985). However, an improved ice core chronology based on methane concentrations demonstrates that suborbital-scale temperature variations occurred in Antarctica prior to their occurrence in Greenland (Blunier and Brook, 2001). Sediment cores with connections to both hemispheres through paired planktic and benthic records confirm this was the case for water masses as well, with changes in the Southern Hemisphere (or Antarctic Bottom Water) preceding those in the Northern Hemisphere (or NADW). (Charles et al., 1996; Shackleton et al., 2000). While the origin and cause of these events is unknown, tropical climate variability may be implicated (Cane 1998).
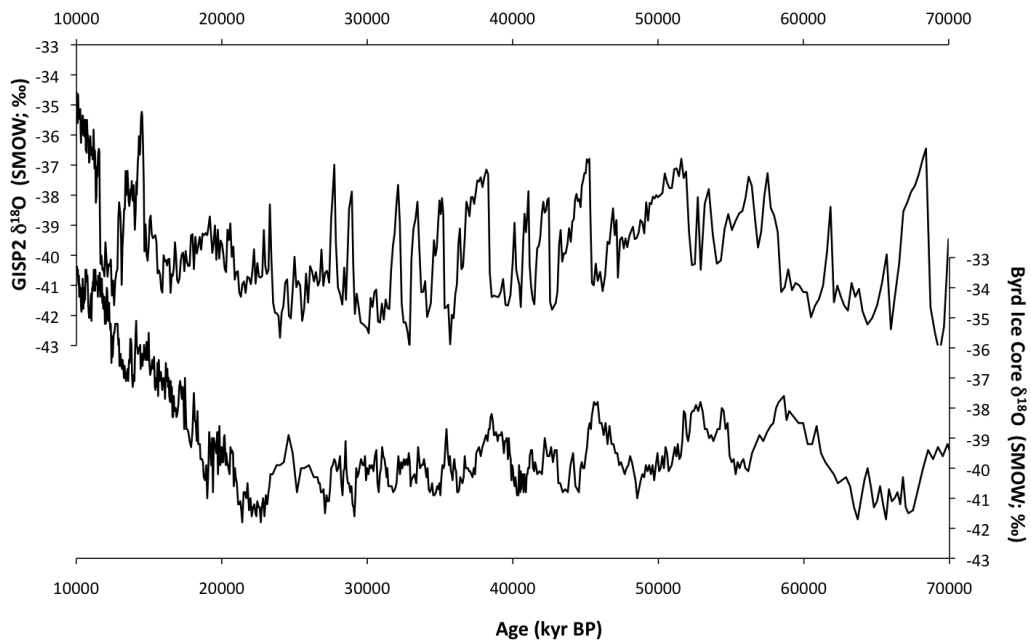
Figure 2. Greenland (GISP2) and Antarctic (Byrd) ice core δ¹⁸O records demonstrating millennial scale events during the last glacial period. From Blunier and Brook 2001.
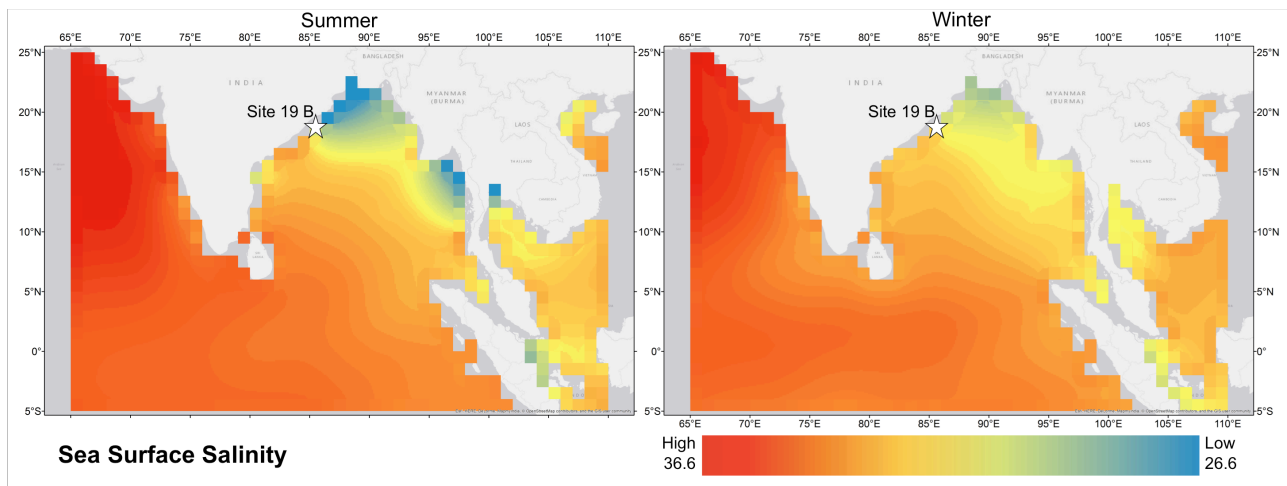
Figure 3. Map of the Bay of Bengal with sea surface salinities averaged between the summer months (JAS) and winger months (JFM), demonstrating the seasonal variability at the core site, labeled.

There is evidence that these suborbital climate events also occurred in the monsoon region (e.g., Wang et al., 2001), therefore, any hypothesis that attempts to explain millennial scale events must include a mechanism for changes at low latitude as well. Well-dated, high-resolution records of $\delta^{18}O$ in Chinese speleothems suggest that suborbital-scale changes in the intensity of the East Asian monsoon may have occurred synchronously with changes in the North Atlantic (Cheng et al., 2009; Wang et al., 2001; Yuan et al., 2004). While the East Asian monsoon system is not necessarily a perfect analogue to the Indian monsoon, this synchronicity implies a mechanistic atmospheric link between the Asian monsoon and Greenland.

Although an atmospheric link is undetermined, a multitude of evidence suggests that monsoon intensity does indeed fluctuate on millennial timescales (e.g., Kudrass et al., 2001; Schulz et al., 1998). Due to the highly variable surface salinities caused by the monsoon, the Bay of Bengal is an ideal location to use salinity tracers, as incorporated into planktic foraminifera, to quantify monsoonal intensity. Kudrass et al. (2001) was the first study to identify suborbital variability in monsoon intensity throughout the last glacial period using this principle; however their record lacks an independent age control, making it difficult to compare to other records. Numerous recent studies dated with radiocarbon and using an independent temperature proxy to isolate the component of the $\delta^{18}O_c$ signal that is due to salinity have found evidence of the Younger Dryas (Govil and Naidu, 2011; Rashid et al., 2011, 2007; Schulenberg, 2011); however these studies do not extend beyond 32 ka.

Two dated records do extend well into the last glacial period: one from the equatorial Indian Ocean and one from the Arabian Sea (Ahmad et al., 2012; Schulz et al., 1998). Both reveal millennial scale events; but these studies lack a temperature control to isolate the seawater salinity signal for an estimate of freshwater fluxes. Nevertheless, both studies concluded that

warm (Dansgaard-Oshegar) events over Greenland corresponded to a strengthening of the summer monsoon, and cooling corresponded to a weakening of the monsoon.

While mechanisms for atmospheric links are unknown, one prominent hypothesis states that changes in the intensity of the Asian monsoon are linked to changes in climate conditions of the Southern Hemisphere (Rohling et al., 2009). This connection is observable in at least one speleotem record as well (Cai et al., 2006). Changes in the global ocean circulation could be both a mechanism and a tracer for the propagation of climate signals on both orbital and suborbital timescales. Antarctic Intermediate Water (AAIW) is a water mass that originates in the Southern Ocean and circulates northward in the Atlantic, Pacific, and Indian Oceans. Intensity of AAIW is thought to respond to (or cause) Southern Hemisphere millennial scale climate events during glacial periods, then referred to as Glacial Antarctic Intermediate Water (GAAIW) (Pahnke et al., 2008). Benthic foraminiferal nutrient proxies at a core site in the Southwest Pacific trace the abrupt intensification of AAIW in conjunction with NADW shutdown (Pahnke and Zahn, 2005). This invigoration may have allowed AAIW to reach 35° farther north in the Atlantic than it does today (Rickaby and Elderfield, 2005).

There may be evidence that this occurred in the Indian Ocean as well. High-resolution records of denitrification using nitrogen isotopes in the Arabian Sea reveal a GISP-like variability (Altabet et al., 2002). The fractionation of nitrogen isotopes is controlled by denitrification, an anaerobic reaction; thus the $\delta^{15}N$ covaries with the oxygen minimum zone of the subsurface water mass (Altabet et al., 1995). One way to interpret this relationship is as evidence of an atmospheric link between Greenland and the monsoon (Bryan et al., 2010; Jung et al., 2009); where strong monsoon-related winds cause upwelling, which enhances productivity and leads to oxygen depletion of the mid-water column, allowing for more denitrification.

However, another interpretation is possible. The extent of the oxygen minimum zone may not be controlled solely by monsoons, but by ventilation of the intermediate-depth water mass. The oxygen minimum zone in the Arabian Sea extends from 100-1000 m depth (Sarma, 2002). A model by Sarma (2002) quantifies vertical exchange due to upwelling as only one third of the water mass exchange, with lateral advection dominating. Furthermore, any increased ventilation from atmospheric forces is dampened by an increase in oxygen consumption due to the increased production from the upwelling nutrients (Sarma, 2002). Most importantly, the water mass origin of the OMZ is from warm marginal seas, already depleted in oxygen (Olson et al., 1993; Pichevin et al., 2007). Thus, any changes in the extent or intensity of the OMZ may reflect changes in the subsurface water mass ventilation, not monsoon intensity (Sarma, 2002). Periodic invigorations of GAAIW may have allowed this water mass to enter the Arabian Sea, ventilating it with oxygen, decreasing the size of the OMZ, and causing a drop in denitrification (Pichevin et al., 2007). Because these events originate in the Southern Hemisphere, they would be in opposite phase to those in Greenland.

Periodic influxes of more-oxygenated waters also help explain high-resolution organic carbon (TOC) records in the coastal Arabian Sea, which, like denitrification records, are highly correlated to the Greenland ice cores (Deplazes et al., 2013; Schulz et al., 1998; Ziegler et al., 2010). Organic carbon accumulation is dependent on both production and preservation. Thus, the organic carbon data are consistent with either high productivity during Dansgaard-Oshegar events (warming over Greenland), and/or a more intense oxygen minimum zone preserving the carbon-rich sediments. The preservation hypothesis applies to aragonite preservation records as well as organic carbon (Böning and Bard, 2009). While not all studies agree that preservation is

the primary driver of the organic carbon records (Caley et al., 2013), the intensity of the oxygen minimum zone would be lessened if GAAIW entered the Arabian sea at intermediate depths.

There is also support for intermittent expansion of GAAIW from direct studies of intermediate-water ventilation in the Arabian Sea. Peaks in intermediate-depth ventilation, represented by higher benthic $\delta^{13}C$, were found to be anti-phase with Greenland temperature fluctuations as linked by planktic monsoonal signals off the Somalia Coast (Jung et al., 2009). Another study found millennial-scale fluxes of $\Delta^{14}C$-depleted (i.e., younger) intermediate waters entering the Arabian Sea coincident with warming events in Antarctica (Bryan et al., 2010). This may point to a Southern Hemisphere control of what were previously assumed to be monsoon records in the Arabian Sea. This could explain the 'Southern 2Hemisphere imprint' observed in some Arabian Sea organic carbon records (Caley et al., 2013). It also leaves open the possibility that the monsoon itself was influenced by the Southern Hemisphere as suggested by Rohling et al. (2009).

Since Southern Hemisphere waters are implicated in the propagation of suborbital scale climate variability (Barker et al., 2009; Caley et al., 2013), it is of importance to constrain the relative timing of atmospheric monsoon events to ocean circulation in the Southern Hemisphere.

Study Objectives

The Asian monsoon is an important component of the global climate, but there is much still unknown concerning the connections, feedbacks, and propagation of climate signals around the globe. The seeming contradiction between the orbital hypothesis and the 8 kyr lag found in many paleomonsoon records has yet to be resolved. Furthermore, the synchronicity between millennial scale changes in monsoon intensity and changes in Greenland temperature (e.g., Wang

et al., 2001) is under scrutiny (Clemens et al., 2010; Rohling et al., 2009). Paleoclimate reconstructions that constrain the timing of these events can help refine the possible causes of the drastic and sudden climate oscillations that occurred during the last glacial period.

The goal of this study is to reconstruct changes in surface and subsurface water properties in the northwest Bay of Bengal. This was accomplished by generating both planktic and benthic foraminiferal records from sediment core NGHP-01-19B, hereafter referred to as "19 B", collected during the 2007 NGHP-01 Expedition (Collett et al., 2008). The planktic data reflect changes in the intensity of the Indian Monsoon, and the benthic data reflect changes in the bottom water chemistry at the core site, which most likely varied with the subsurface water mass associated with large-scale ocean circulation. The portion of this new record examined in this study covers the last 55 to 24 ka, which includes several suborbital events known from ice core and speleothem records.

In order to reconstruct monsoon intensity, a downcore record of changes in the oxygen isotopic composition of surface water ($\delta^{18}O_{sw}$), which varies with rainfall volume, was generated. These $\delta^{18}O_{sw}$ values were obtained by analyzing the oxygen isotopes ($\delta^{18}O_c$) of the calcareous tests of the planktic foraminiferal species *Globerginoides ruber*, which lives within the top 50 m of the ocean surface. Foraminiferal $\delta^{18}O$ ($\delta^{18}O_c$) is a function of both calcification temperature and the oxygen isotopic composition of the water in which calcification occurs ($\delta^{18}O_{sw}$). To separate these signals, Mg/Ca of the *G. ruber* calcite was measured, which is a function of temperature (pH effects are assumed constant). The fluctuations in $\delta^{18}O_c$ due to temperature changes can then be subtracted out, isolating the $\delta^{18}O$ changes that are due to surface salinity changes. Because salinity of the Bay of Bengal is strongly controlled by monsoon precipitation and monsoon-controlled river discharge (see Figure 3), surface salinity is

a proxy for the intensity of the Indian monsoon. However, since *G. ruber* is present throughout the year in the Bay of Bengal, this methodology gives no indication of the seasonality of the freshwater discharge. Rather, the signal is an average of near surface conditions over the time period of accumulation for each sample's 1-cm section of the core; approximately 100 years.

Past variations in the intermediate-depth (1,422 m) water masses were reconstructed using benthic foraminiferal Cd/Ca and $\delta^{13}C$, which vary with nutrient content in the modern ocean and are commonly used as water mass tracers (e.g., Boyle and Keigwin, 1985; Boyle et al., 1995; Charles et al., 1996; Curry and Oppo, 2005; Figures 4-7). The $\delta^{13}C$ was measured in *Cibicidoides pachyderma*, supplemented by *Cibicidoides wullerstorfi*. Both live at the sediment-water interface and incorporate the same fraction of $\delta^{13}C$ into their tests (Curry and Oppo, 2005). Cd/Ca was measured in *Hoeglundina elegans*, a foraminfer that is known to incorporate cadmium with a conversion factor of one, and whose shells are resistant to contaminating metal overgrowths (Boyle et al., 1995).

By using benthic-planktic pairs from the same sediment core, the *relative* timing of surface variations (reflecting changes in the monsoon) and subsurface variations (reflecting changes in the intermediate-depth water mass) will be absolute, regardless of the chosen age model. This tests how changes in the monsoon are temporally linked to changes in ocean circulation.
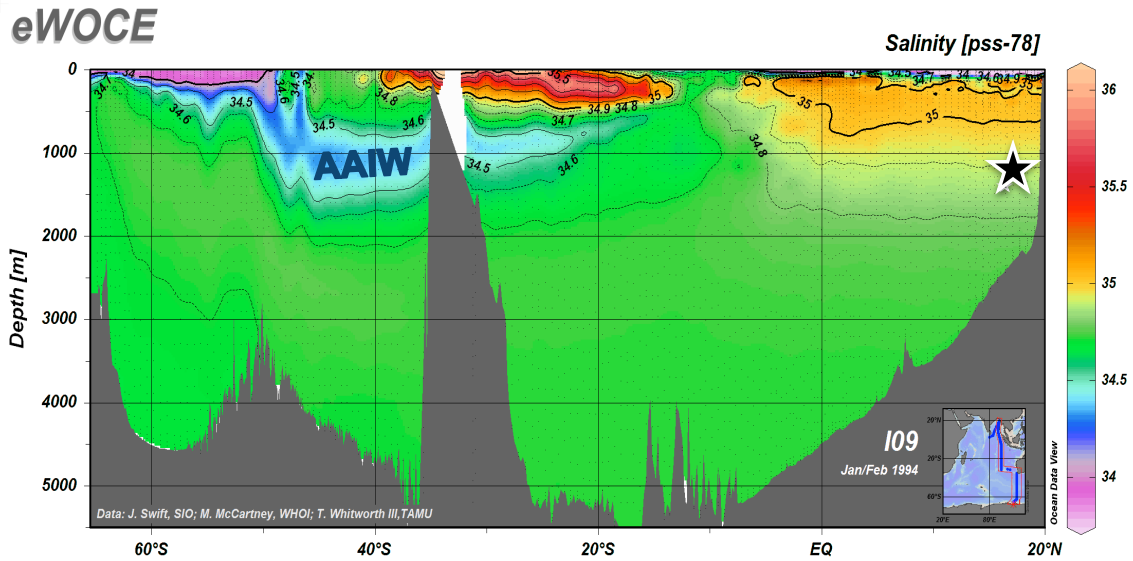
Figure 4. Modern subsurface salinity in the eastern Indian Ocean, demonstrating the current extent of Antarctic Intermediate water. (It extends a bit further in the west). AABW and IDW Indian Deep Water appear green. ITF mixed with RSW and AAIW is the orange surrounding the 19 B core site, which is labeled with a star. Low salinity BBW is visible at the surface of the core site.
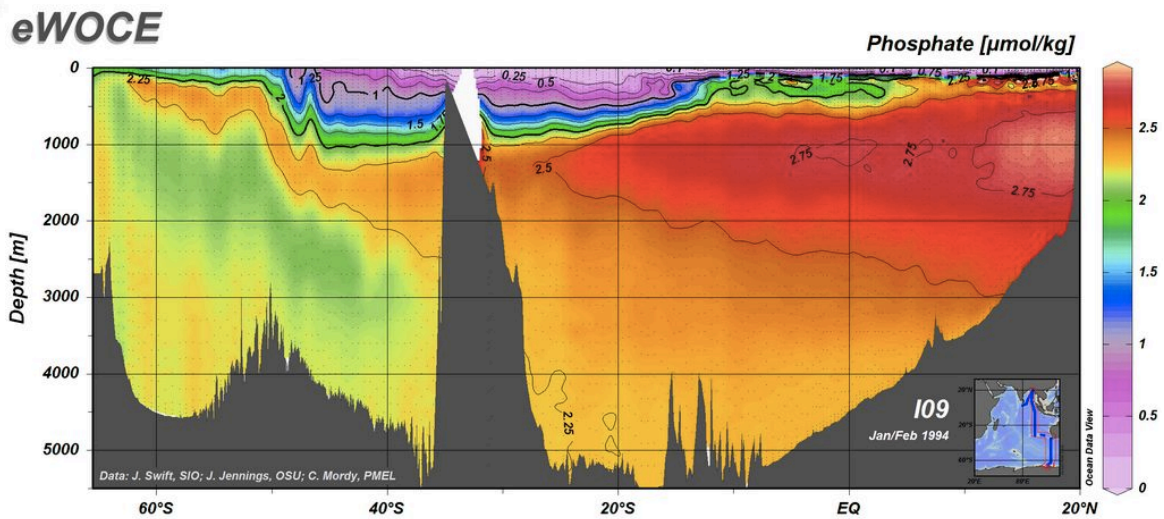
Figure 5. Modern phosphate distribution in the eastern Indian Ocean. Phosphate is high at the core site, which would entail a high cadmium content and a depleted ^{13}C content. The tongue of AAIW is not as distinct in the phosphate field, but is lower in phosphate than the water present at the core site.
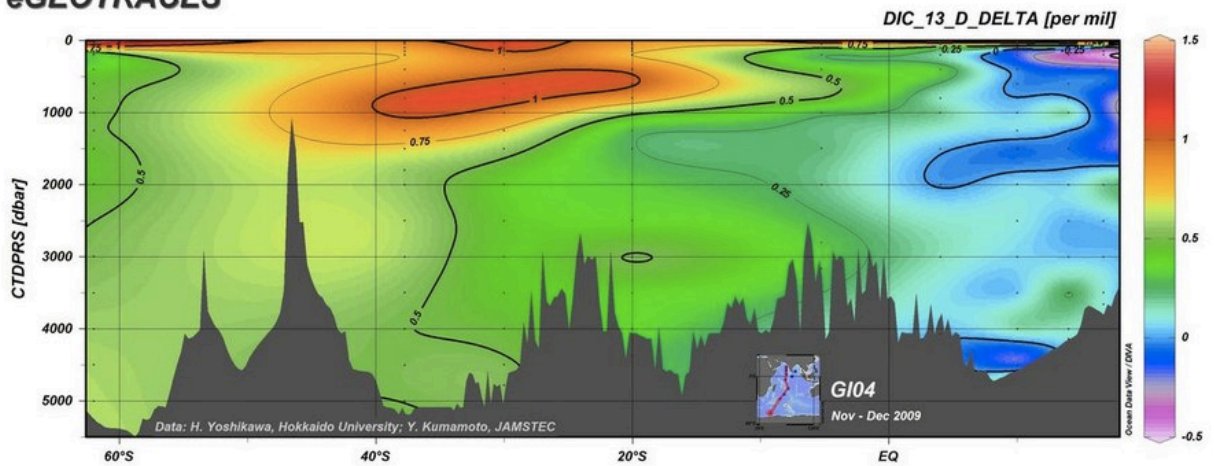
Figure 6 : Modern δ¹³C distribution in the western Indian Ocean. In the modern Indian Ocean, the highest δ¹³C values are from AAIW and surface water (including subtropical convergence water).
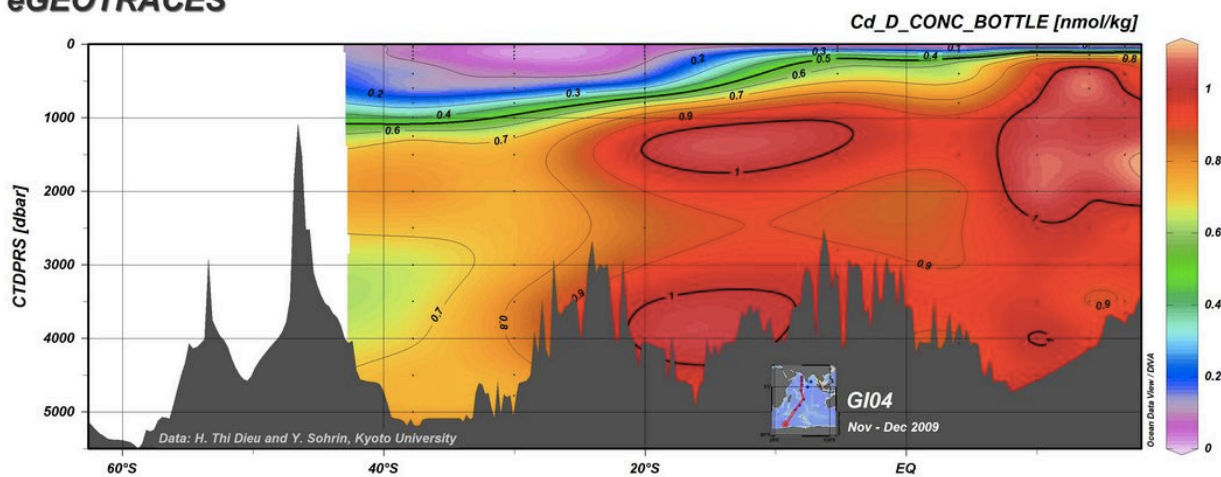
Figure 7 : Modern cadmium distribution in the western Indian Ocean. In the modern Indian Ocean, the highest cadmium values are from aged AABW, south-returning Indian Deep Water, and Red Sea Water.

Oceanographic Setting

The Indian Ocean is quite different from the Atlantic and Pacific because it is landlocked to the north, with the Indian peninsula further dividing the northern Indian Ocean into two separate seas, the Arabian Sea and the Bay of Bengal. This northern land boundary means much of the water in the Bay of Bengal originates from the south. However, inputs from rivers and marginal seas are significant components of the Bay's water content and circulation (Talley et al., 2011).

Trade winds in the northern Indian Ocean reverse seasonally due to the highly seasonal temperature gradient between the Eurasian landmass and the surface waters of the Indian Ocean (Ruddiman, 2001). These winds drive two different modes of surface circulation. During the winter monsoon, the main winds in the northern tropics are the equatorial easterlies, which blow towards the southwest, creating the typical equatorial currents and surface gyres. In contrast, the summer heating of the Eurasian land mass creates an intense atmospheric low over the Tibetan plateau, driving cross-equatorial winds and pouring rain onto the Indian subcontinent. This summer or southwest monsoon causes significant upwelling off the coasts of Oman and Somalia, the waters of which are some of the planet's most productive, and perhaps weak upwelling in the Bay of Bengal as well (Prasanna Kumar et al., 2002).

The salinity of surface water at the 19 B core site varies dramatically in response the Indian monsoon (cf Figure 3). A water mass sourced from the surface and river runoff is created each summer, sometimes called Bay of Bengal Water (BBW) (Tomczak and Godfrey, 2003). Spanning nearly 100 m thick, this lens stretches down into the tropics, bringing the surface salinities down to as low as 25 (Tomczak and Godfrey, 2003). Surface salinities in the Bay of

Bengal barely reach 33 in May before it is once again inundated with fresh water. This meteoric fresh water is lighter in ^{18}O, allowing δ^{18}O of surface-dwelling organisms to be used as a tracer for surface salinity (e.g., Ahmad et al., 2012; Bolton et al., 2013; Govil and Naidu, 2011; Kudrass et al., 2001; Marzin et al., 2013; Rashid et al., 2011, 2007; Schulenberg, 2011).

The deepest water in the Indian Ocean is Antarctic Bottom Water (AABW), but this water mass does not reach far into the Bay of Bengal, which is shallower than 4000 m (Tomczak and Godfrey, 2003). However, warmed AABW does mix into Indian Deep Water (IDW), which is the bulk of water in the Indian Ocean. IDW originates as North Atlantic Deep Water (NADW), which slowly moves northward throughout most of the Indian Ocean, including the Bay of Bengal, from 3800 to 1500-2000 m depth (Tomczak and Godfrey, 2003). The upper portion of IDW (above 2000 m depth) is dominated by a southward return flow (Talley et al., 2011). This old, high-nutrient water mass may contribute to the waters present at the 19 B core site.

Most of the rest of the water in the Bay of Bengal is sourced from Indonesian Intermediate Water (IIW). IIW is an intermediate-depth water mass originating as Pacific Central Water. It passes through the Australasian Mediterranean Sea as Indonesian Through Flow, where it remains relatively fresh at 34.8 (Tomczak and Godfrey, 2003), and enters the Bay of Bengal through point sources around Indonesia. There, IIW flows westward across the Indian ocean at thermocline levels, remaining between 100 and 400 m depth in its core, and reaching a maximum depth of 1000 m (Tomczak and Godfrey, 2003). The westward stream of the IIW serves an important role in extending the equatorial hydrological front to several hundred meters depth, almost entirely blocking water exchange between hemispheres in the Eastern Indian Ocean. (However, the monsoon-forced reorganization of currents seasonally aids in the exchange of surface waters between the southern and northern Indian Ocean) (You, 1998). After traversing

to Sri Lanka, about 60% of the IIW then enters the Bay of Bengal and circulates in a clockwise motion at thermocline levels (You, 1998). The contribution of IIW to the Bay at depths exceeding 1000 m is not known.

In the Arabian Sea, a warm, high-salinity intermediate-depth water mass is created by the outflow of Red Sea and Persian Gulf waters. This Red Sea Intermediate Water (RSW) has a density that is so high that it sinks to 400-1400 m depth (Talley et al., 2011) and fills much of the Arabian Sea. This water is advected around the southern tip of India and enters the Bay of Bengal from the west during the winter monsoon season, where it circulates clockwise, like the IIW (You, 1998). Because this water reaches a depth of 1400 m as it enters the Bay of Bengal, some influence of RSW is likely present at our core site.

Another intermediate-depth water mass present in the Indian Ocean is Antarctic Intermediate Water (AAIW), which is labeled in Figure 4. AAIW is present in all three major oceans, and is considered to be an important element of global circulation because it is the main water mass at thermocline depths in the southern hemisphere, and so potentially affects a large number of factors such as temperature gradients and nutrient availability from wind-curl-induced upwelling (Hendry et al., 2012; Olson et al., 1993; Sarmiento et al., 2004). Modern AAIW in the Indian Ocean originates in the southwestern Atlantic Ocean, where Atlantic AAIW forms at the confluence of currents, giving Atlantic AAIW a different signature than that of the southeastern Pacific (Talley et al., 2011). Thus, the AAIW present in the Indian Ocean is older than AAIW in other oceans (Talley et al., 2011).

In the South Indian Ocean, AAIW is found from 1500-1000m depth, just above Indian NADW (Tomczak and Godfrey, 2003). In modern times, northward-flowing AAIW rarely reaches beyond 10°S in the east, blocked by the IIW flowing westward and south; and does not

reach beyond 5°N in the Arabian Sea, where it crosses the equator in a western boundary current (You, 1998). As it moves northward, AAIW shoals over RSW and southward-flowing IDW. A small percentage of AAIW which enters the equatorial Indian Ocean moves eastward along the equator and enters the Bay of Bengal via a western boundary current, which circulates clockwise around the Bay with the IIW (You, 1998). This contribution is why waters at intermediate depth in the Bay of Bengal are fresher than those in the Arabian Sea (You, 1998). However, the AAIW shoals to a depth of 500-700m by the time it reaches the Bay (You, 1998), meaning it does not reach our core site (1422 m depth).

Today, AAIW is a small contributor to intermediate depth waters in the Bay of Bengal (You 1998). However, the few studies that have examined intermediate-depth water masses in the Bay of Bengal during the last glacial maximum may indicate AAIW extended into the Bay of Bengal at times during the last glacial period: The δ^{13}C gradient of waters at intermediate depth (1200-1600 m) suggest increased ventilation in the Arabian Sea which may indicate a stronger presence of cold Glacial Antarctic Intermediate Water (Jung et al., 2009; Kallel et al., 1988)). Furthermore, an analysis of cadmium content in the eastern Bay of Bengal indicates that the intermediate waters (1357 m) during the last glacial maximum were nutrient depleted compared to the deep water at that time (Boyle et al., 1995).

Waters deeper than 2000 m appear to have been nutrient enriched during the glacial maximum compared to the modern (Boyle et al., 1995; Kallel et al., 1988; Naqvi et al., 1994), which may indicate slower renewal of Indian Deep Water. These studies depict how subsurface water masses in the Bay during the last glacial period may have differed from the Holocene.

Previous studies from the core 19 B site illuminate the processes occurring in the Bay of Bengal relevant to this study. The sediment supply to the core site appears to be from monsoon-

driven weathering (Phillips et al., 2014). The stable isotopes of planktic foramifera from 22 ka to present suggest an overall weaker monsoon during the last glacial period compared to the modern (Schulenberg, 2011), consistent with many other monsoon records. On a longer timescale of 110 ka to present, changes in monsoon intensity do not seem to be the most salient effect on productivity; rather, calcium carbonate mass accumulation rates peaked from 70-10 ka (Phillips et al., 2014). Phillips et al. (2014) suggest that freshwater stratification rather than wind-driven upwelling is the main cause of carbonate production in the northwestern Bay of Bengal (Phillips et al., 2014). On even longer timescales of 4 million years, productivity at site 19 may be linked to nutrient availability from Indonesian Through Flow waters (Cawthern et al., 2014).

Materials and Methods

Core NGHP-01-19B (18°58.6568'N, 85°39.5202'E; 1,422 m) was recovered from the Mahanadi Basin of the Bay of Bengal on 7 August 2007 during the first expedition of the Indian National Gas Hydrate Program (Collett et al., 2008). The core is 26.3 meters in length including NGHP-01-19B-01H through NGHP-01-19B-03H. Core NGHP-01-19B was cut into 150-cm-long sections (NGHP-01-19B-1H-1, 1H-2, etc) and the working and archive halves are stored in the Woods Hole Oceanographic Institution Core Repository.

Initial sampling for stable isotope analysis of core NGHP-01-19B-1H was performed by Steve Philips, PhD student of UNH, at an interval of every 30 cm (Phillips et al., 2014). Further sampling from 8 to 730 cmbsf was conducted at an interval of every 8 cm by Sarah Schulenberg, M.S. student of UNH (Schulenberg, 2011). Approximately 1 cm x 1 cm x 2.5 cm volumes of sediment were sampled from the core and freeze dried before being washed.

I further sampled the core to increase the resolution to every 4 cm for the interval from 342 to 606 cmbsf. In this case, approximately 2 cubic cm of sediment was removed and the samples were not frozen or freeze-dried. The samples were gently rinsed with warm tap water through a 0.63 micron sieve, and dried in an oven at 50°C for several hours. This process of rinsing and drying was repeated until the foraminiferal samples were visually free of clay. The samples were then transferred to glass vials for storage.

Picking of the foraminiferal samples was performed by sieving the washed, dry samples through a series of sieves in order to separate certain size fractions. The pertinent size fraction was then sprinkled into a tray, and species determinations and picking were done using a compound light microscope. Four species were selected: The planktic species *Globerginoides ruber* (white) from the 212-250 μm size fraction; and the benthic species *Cibicidoides pachyderma, Cibicidoides wuellerstorfi*, and *Hoeglundina elegans* from all size fractions >212 μm. Abundances did not allow for *C. pachyderma* or *C. wuellerstorfi* to be collected from every sample; but *G. ruber* and *H. elegans* were generally abundant and ubiquitous.

Where abundances allowed, approximately 100 μg of benthic foraminiferal *C. pachyderma* tests (5-10 individuals) were selected, weighed, and folded into envelopes and sent to the University of California at Santa Cruz Stable Isotope Laboratory for $\delta^{18}O$ and $\delta^{13}C$ analysis. Where abundances were scarce, *C. wuellerstorfi* tests were used to supplement. These two benthic species have been found to have similar stable isotope values (Slowey and Curry, 1995). The analytical precision of the Santa Cruz stable isotope mass spectrometer system is ± 0.08 ‰ based on repeated analyses of the NBS-19 standard (Andreasen, 2008). Planktic foraminiferal *G. ruber* samples consisted of 50 individual tests from the 212-250 μm size fraction. Care was taken to find whole, non-deformed specimens of the s.s. morphotype when

available (Steinke et al., 2005). If abundances were scare, s.l. morphotypes were incorporated. In seven samples, abundances were still too low, and as few as 40 individuals were used, carefully noted to be handled delicately.

These 50 individuals were weighed, then gently crushed between two glass slides under a compound light microscope and the pieces were stirred and homogenized. Then, separate aliquots were allocated, with about 1/5 of the material (~70 μg) placed in envelopes for stable isotope analysis as above, and 4/5 of the material placed in leached polyvials for trace/minor element cleaning. Where replicates were needed, a few planktic stable isotope samples consisted of only 10 individuals (See Table 6 for details).

Cleaning *G. ruber* for magnesium/calcium analysis was done in the trace metal clean laboratory of Dr. Linda Kalnejais, UNH. The protocol of Boyle and Keigwin (Boyle and Keigwin, 1985) was followed with the oxidative and reductive steps reversed (Boyle and Rosenthal, 1996). The crushed foraminiferal pieces were first treated with methanol to remove clays; then treated with a reducing agent (ammonium hydroxide, citric acid, and anhydrous hydrazine) to remove any metal oxide contamination; then treated with an oxidizing agent (sodium hydroxide and hydrogen peroxide) to remove any organic materials; and finally polished with dilute trace metal-clean nitric acid to remove any remaining contaminating phases.

The clean samples were then analyzed on the Element 2 single collector Inductively Coupled Plasma Mass Spectrometer at the Woods Hole Oceanographic Institution. This was done in aqueous phase, which is optimal for instrument sensitivity and accuracy (Woods Hole Oceanographic Institution, 2012), by dissolving samples in 2% nitric acid, and further diluting if necessary for optimal concentrations. The *G. ruber* calcite was run at 50 ppm Ca and simultaneous intensities of calcium, magnesium, and manganese were measured according to the

protocol of Rosenthal (Rosenthal et al., 1999). A standard curve of various standard concentrations was run to correct for the Ca matrix effect and to convert intensity into Mg/Ca. Additionally, three consistency standards were run with Mg/Ca values of 1.65 mmol mol^{-1}, 3.34 mmol mol^{-1}, and 4.99 mmol mol^{-1}. The long-term standard deviations of these standards are ±0.04 mmol mol^{-1}, ±0.09 mmol mol^{-1}, and ±0.15 mmol mol^{-1} respectively (Schulenberg, 2011). Mn/Ca ratios were monitored to ensure that the samples were free of metal oxides.

Magnesium/calcium ratios were converted to calcification temperature using the calibration from Dekens et al. (Dekens et al., 2002):

$$Mg/Ca \ (mmol \ mol^{-1}) = 0.38 \ exp \ [0.09 * SST \ (°C)]$$

The $\delta^{18}O$ of sea water was then calculated from the $\delta^{18}O$ of the calcite and the sea water temperature (T) using the equation from Mülitza (Mulitza et al., 2003):

$$\delta^{18}O_{sw} = \delta^{18}O_c + (T-14.20)/4.44$$

In a similar manner as above, benthic *H. elegans* specimens were picked from all size fractions >212 μm. Approximately 500 μg of material (about 10 individuals) was chosen by selecting unbroken, visually well-preserved specimens (free of any visible indications of dissolution). The individuals were then gently crushed between glass slides and subjected to the same chemical treating process as above (Boyle and Keigwin, 1985; Boyle and Rosenthal, 1996)

The clean samples were also analyzed on the Element 2 ICP MS at WHOI. The *H. elegans* aragonite was run at 200 ppm Ca rather than 50 ppm, in order to increase the signal to noise ratio of the trace concentrations of Cd. Simultaneous intensities of calcium, magnesium, manganese, and cadmium were measured as above (Rosenthal et al., 1999). A standard curve was again used to correct for the Ca matrix and the Mn/Ca levels were measured to ensure pure samples.

Cadmium data are converted from mmol mol^{-1} Ca to Cd$_w$ (nmol kg^{-1}) using the

distribution coefficient from Boyle (1995), which assumes a constant Ca sea water concentration.

The cadmium levels in *H. elegans* have a conversion factor of one to seawater concentration

(Boyle et al., 1995).

The radiocarbon analyses were performed by the National Ocean Sciences Accelerator

Mass Spectrometry Facility (NOSAMS). Six samples were picked for planktonic foraminifera

and analyzed on an accelerator mass spectrometer (AMS) at the Woods Hole Oceanographic

Institution. See Table 1 for details on foraminifera species.

Lagged correlation analysis of the resultant time-series was performed with a MATLAB

code. This code creates an interpolation between the data points and measures the correlation (r

value) present between two data sets at each interpolated time point. The highest absolute value

of r then represents the highest possible degree of correlation between the two data sets.

Age Model

The age model for the relevant section of core 19 B was determined using radiocarbon

and benthic oxygen isotopes (Table 1; Figure 8). Four AMS radiocarbon dates are from

previously published studies Phillips et al. 2014 and Schulenburg 2011, including samples from

the companion core 19 A, whose depths are adjusted 3.8 cm based on magnetic susceptibility

correlation (Schulenburg 2011, Phillips et al. 2014). The radiocarbon dates are converted to years

before 1950 (BP) using the Calib 7.0 program (Stuvier and Reimer, 1993), calibrated with the

Marine13 dataset. No further reservoir correction beyond 400 years was added. The final age

was determined by taking the mean between the resulting 1-σ range and rounding to the nearest

decade. Two radiocarbon data points (596.5 cmbsf and 618.5 cmbsf) were not used because the

ages were older than the Calib 7.0 program could calibrate. A third (514.5 cmbsf) was rejected

for severe departure from linear interpolation between the surrounding age markers. The age model for the lower part of the core was determined by matching benthic oxygen isotopes reported in Philips et al. 2014 to a SPECMAP model (Lisiecki and Raymo, 2005).

If a linear interpolation is used, then the sedimentation rates range between 4.1 and 10.1 cm/kyr, with a mean sedimentation rate between the two end members of the dataset of 8.1 cm/kyr (See Table 2; Figure 8).
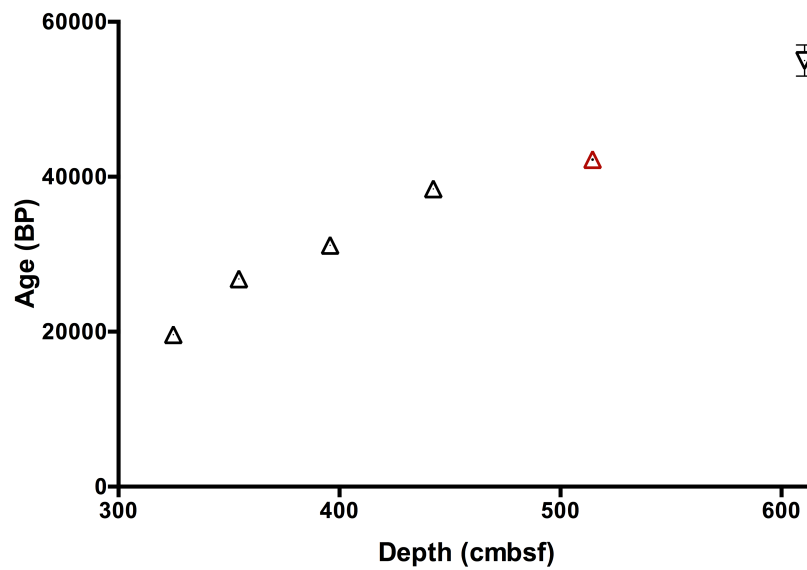
Figure 8: Age Model for Core 19 B. Black triangles are mean AMS radiocarbon dates, calibrated as shown in Table 1. Error bars are smaller than the plotted symbol. The red triangle is the rejected radiocarbon date. The inverted triangle is the benthic isotope age date (see Table 2).

Results

Planktic Data

Stable isotope compositions ($\delta^{13}C$ and $\delta^{18}O$) were analyzed in both planktic and benthic foraminifera, from 330-611 cmbsf. The sampling interval is approximately every 4 cm.

The planktic foraminiferal $\delta^{18}O$ values range from -0.99‰ to -2.00‰ with a mean of -1.44‰ (Figure 9, Table 4). The minimum values are generally present in the upper portion of the core, (342.5-410.5 cmbsf), with the maximum values at excursions at 526.5 and 546.5 cmbsf. One data point (458.5 cmbsf) was determined to be an outlier and will be excluded in subsequent discussion. Eight replicates and two triplicates were measured; all remain within 0.3‰ of each other.

Planktic foraminiferal $\delta^{13}C$ values range from -0.12‰ to 1.07‰, with a mean of 0.60‰ (Figure 10, Table 4). The overall trend is linear with the lowest value at 346.5 cmbsf and the highest value is at 602.5 cmbsf. One measurement (426.5 cmbsf) was determined to be an outlier and will be excluded in subsequent discussion. Eight replicates and two triplicates were measured; all remain within 0.3‰ of each other.

The Mg/Ca data are from the homogenized *G. ruber* samples. There is no significant trend; the values remain near the average value of 3.7 mmol mol^{-1} (Figure 11, Table 5). The highest value at 398.5 cmbsf is considered an outlier and excluded from subsequent discussion. Eight replicates were measured; all remain within 0.38 mmol mol^{-1} of each other, which equates to 1.1 °C, with an average replication of 0.2 mmol mol^{-1} (0.6 °C).
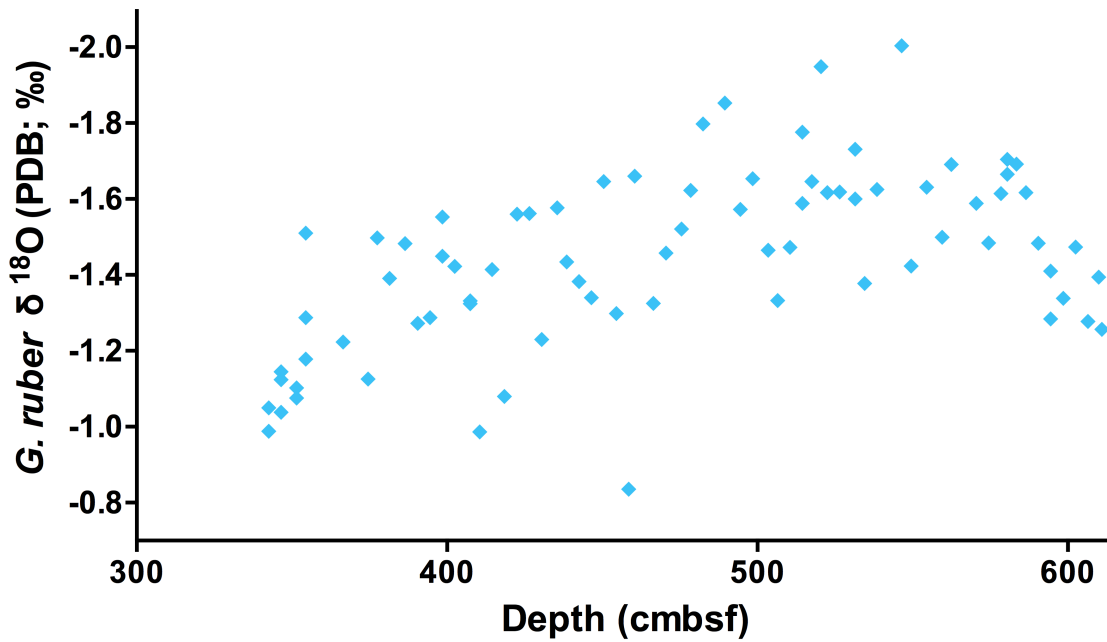
Figure 9: Planktic δ¹⁸O (‰) of *G. ruber* from core NGHP-01-19B versus depth.
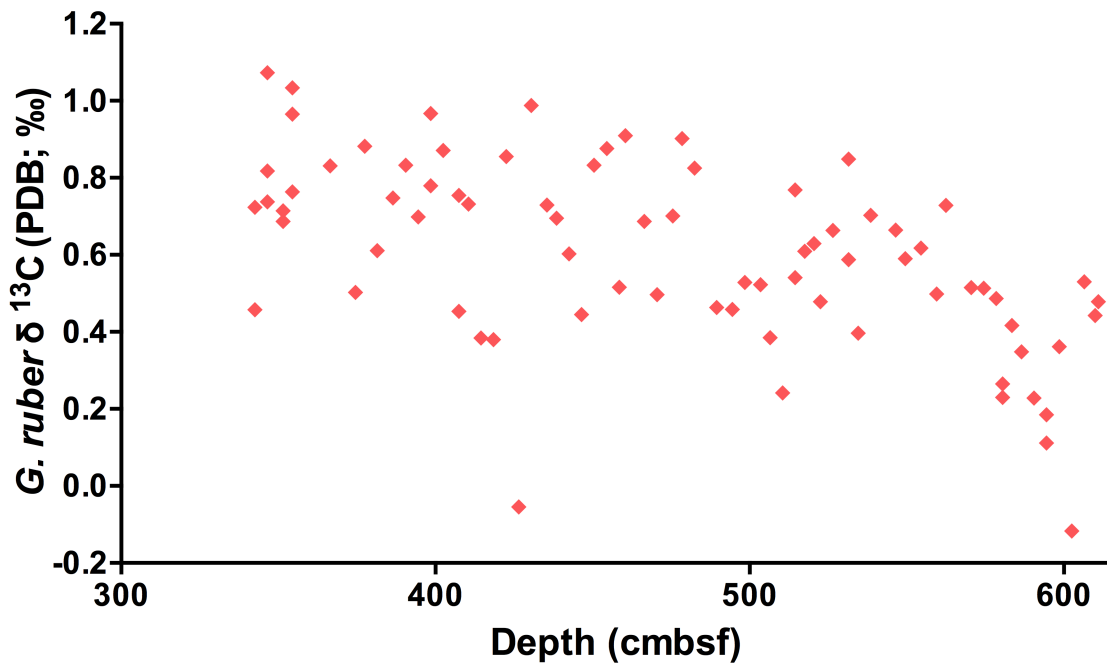
Figure 10: Planktic δ¹³C (‰) of *G. ruber* from core NGHP-01-19B versus depth.
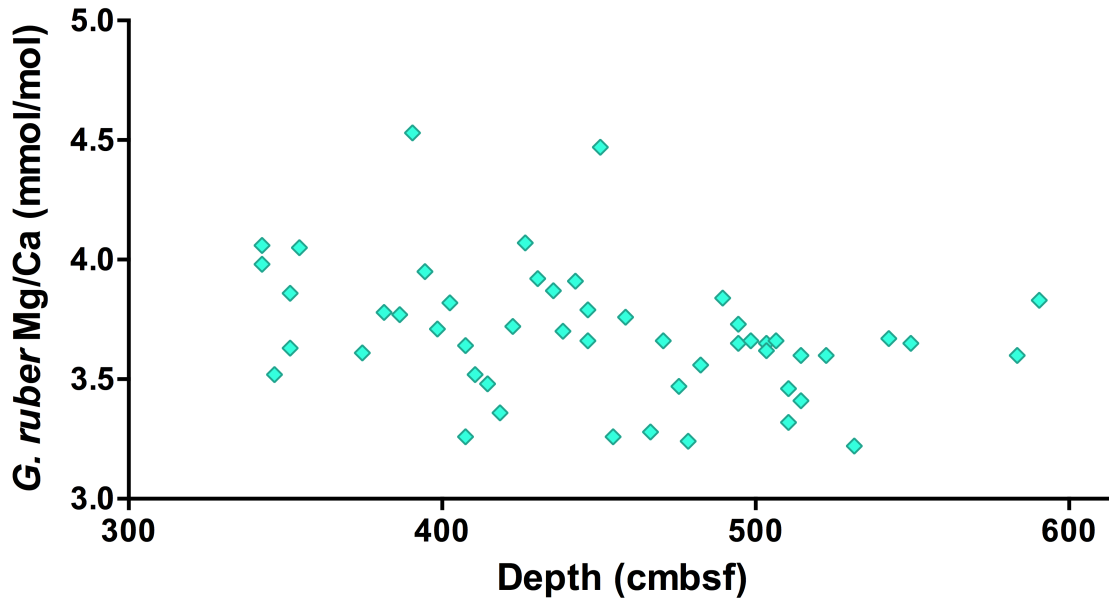
Figure 11: Mg/Ca of *G. ruber* from core NGHP-01-19B versus depth.
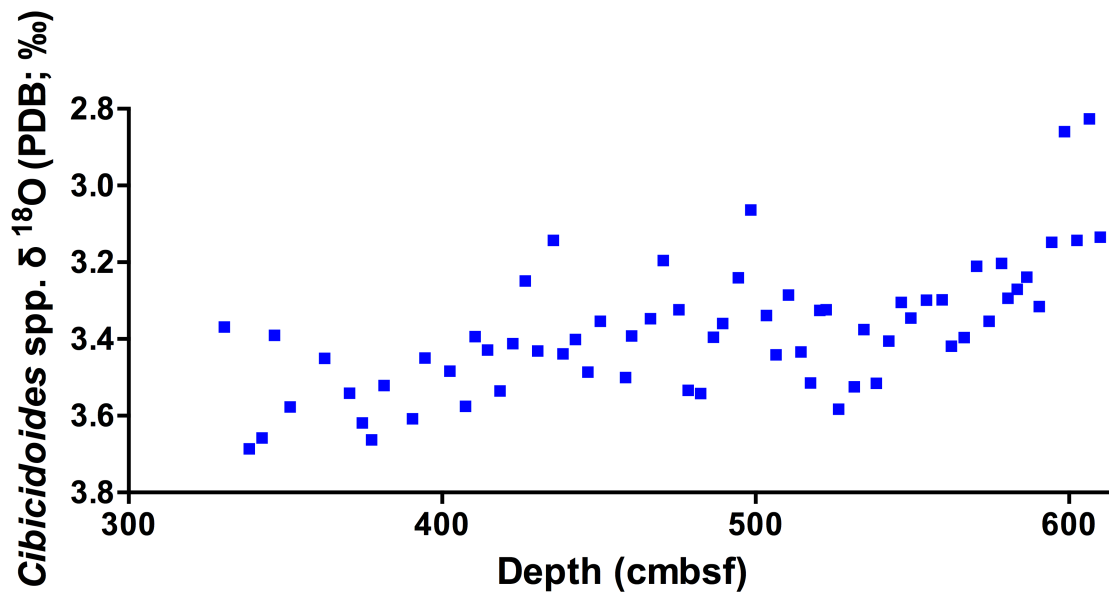
Figure 12: Benthic δ^{18}O (‰) of *Cibicidoides* spp. from core NGHP-01-19B versus depth.
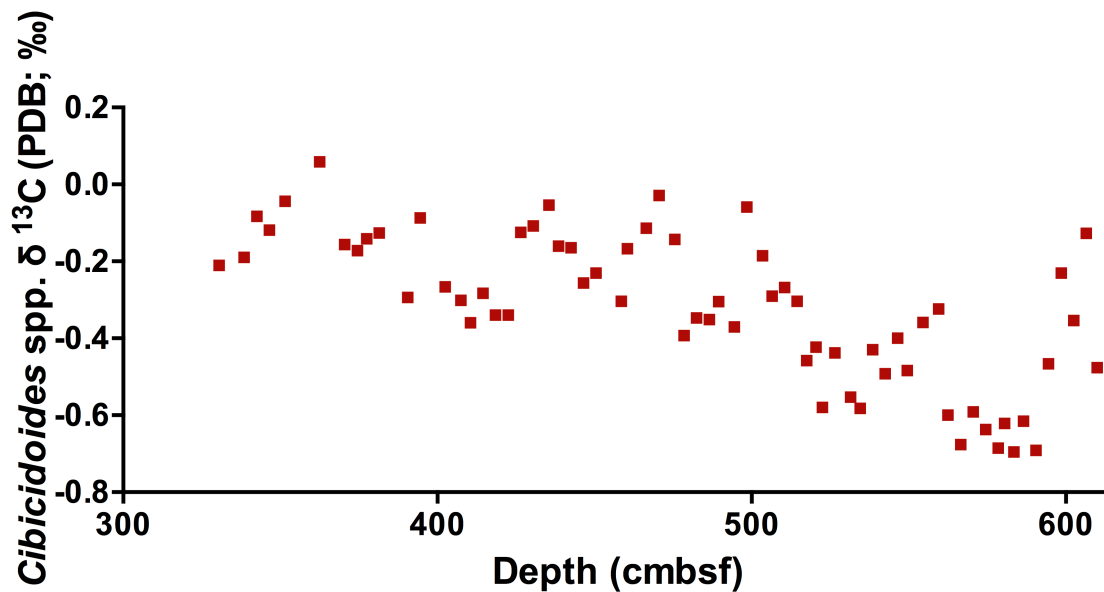
Figure 13: Benthic δ¹³C (‰) of *Cibicidoides* spp. from core NGHP-01-19B versus depth.
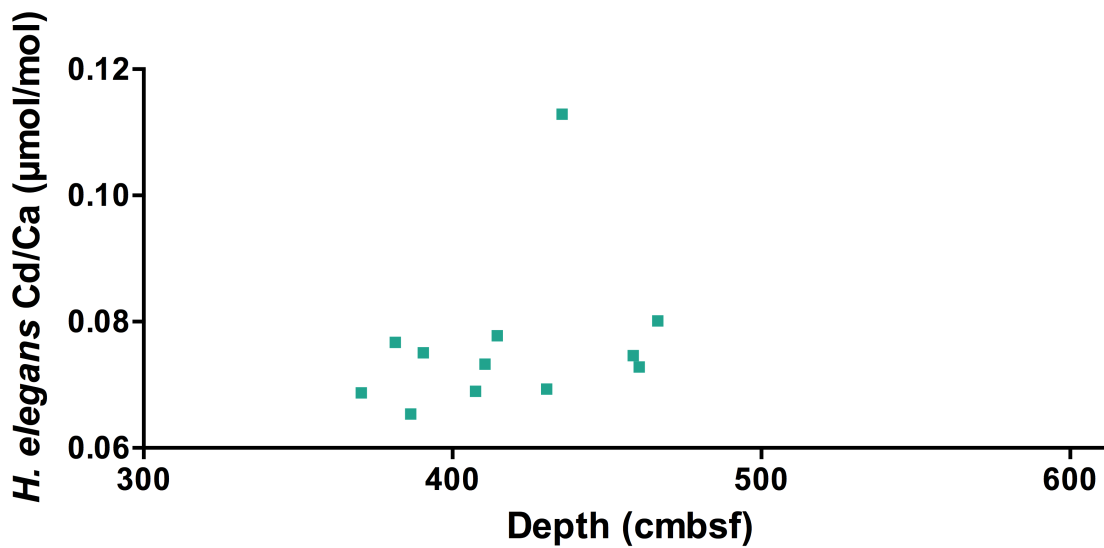
Figure 14: Cd/Ca (mol mol⁻¹) of *H. elegans* from core NGHP-01-19B versus depth.

Benthic Data

The benthic $\delta^{18}O$ values range from 2.83‰ to 3.69‰ with a mean of 3.38‰ (Figure 12). The overall trend is roughly linear with the highest value at 338.5 cmbsf and the lowest value at 606.5 cmbsf. No replicate analyses were conducted.

The benthic $\delta^{13}C$ values range from -0.70‰ to 0.06‰ with a mean of -0.32‰ (Figure 13). The trend is roughly linear with the highest value at 362.5 cmbsf and the lowest value 583.5 cmbsf. No replicates analyses were conducted.

The Cd/Ca data are from only a subset of the foraminiferal samples. The values range from 0.065 to 0.080 µmol mol^{-1} with a mean value 0.073 mmol mol^{-1}, excluding one data point at 435.5 cmbsf as an outlier (Figure 14).

Conversion from $\delta^{18}O_c$ to $\delta^{18}O_{sw}$

The near-surface $\delta^{18}O_{sw}$ values seen in subsequent figures are temperature corrected, calculated from the planktic $\delta^{18}O_c$ and the Mg/Ca-derived temperatures using the equation from Mülitza (2003) (See Figure 15). For samples where $\delta^{18}O_c$ was measured but had no corresponding Mg/Ca measurement, an average value was used.

Ice-corrected $\delta^{18}O_{sw-ic}$ values were also generated by subtracting the influence of global fluctuations in $\delta^{18}O$ associated with sea-level changes from the temperature-corrected $\delta^{18}O_{sw}$. The sea level values are taken from Siddall et al. (Siddall et al., 2003) and the conversion factor of 0.0083‰ m^{-1} sea-level from Adkins et al. (Adkins et al., 2002). We acknowledge, however, the inherent uncertainty involved in the method of Siddall et al. (2003), which used Red Sea salinity as a monitor of sea level; as well as the uncertainty in the dating of each record. In any

case, the adjustment is small enough that the general shape is unchanged, so the interpretation

remains the same with or without the correction (Figure 15). Therefore, for the following graphs

and analyses, only the temperature-corrected $\delta^{18}O_{sw}$ is used. Similarly, no correction for global

ice volume is made in the presented benthic $\delta^{18}O$.
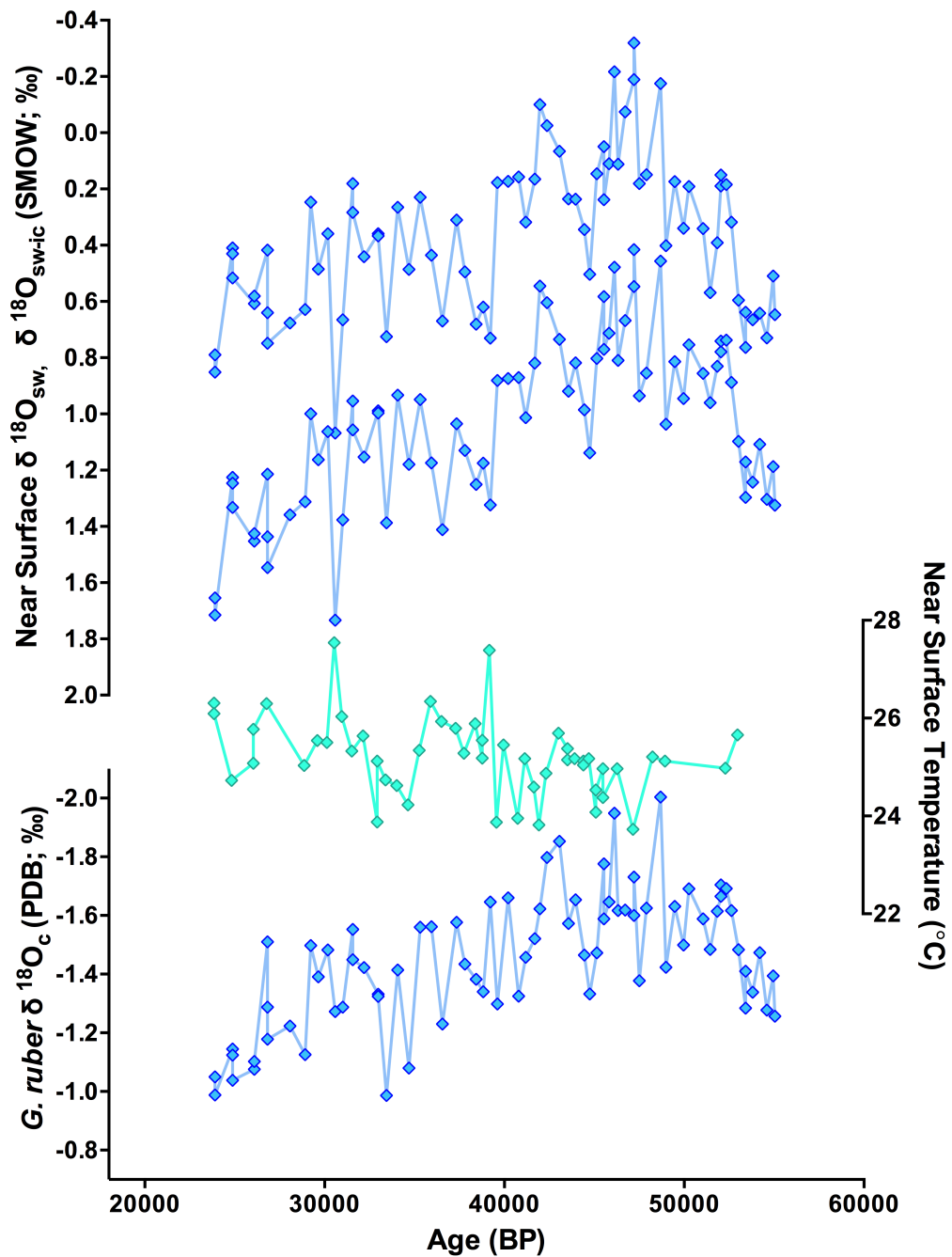
Figure 15: Core NGHP-01-19B $\delta^{18}O_{sw}$ **of** *G. ruber* **(PDB; ‰); Mg/Ca-derived near-surface temperatures; near-surface seawater** $\delta^{18}O_{sw}$ **(SMOW; ‰) from** *G. ruber*, **corrected for temperature; and near-surface seawater** $\delta^{18}O_{sw\text{-}ic}$ **(SMOW; ‰), corrected first for temperature then for global ice volume using high-resolution sea level records from Siddall et al. (2003) and conversion from Adkins et al. (2002).**

Processed Results

The near-surface seawater temperatures display an overall trend of warming from 55 ka to 24 ka which is very slight, with the mean temperature rising from 24.9 to 25.9 °C (Figure 16). Superimposed on this trend are fluctuations, with low temperatures of ~23.8°C at approximately 47, 41, and 33 ka. High temperatures of ~26°C are present at 53, 43, 36, and 27 ka. Two extremely high peaks in SST of over 27 °C are seen in the record at 31 and 39 ka. Both of these events are preceded by cool events, meaning the warming was very sharp, with the more extreme event representing a warming of 3.5°C in just 500 years. However, it is important to note that these two warm events are represented by single data points, and it is possible that these points are anomalous and do not represent real climatic excursions.

The near surface $\delta^{18}O_{sw}$ record is presented with a locally weighted smoothing curve to highlight the millennial-scale variability present. (Figure 16). The $\delta^{18}O_{sw}$ reflects the freshening of the surface waters of the Bay of Bengal, with lower $\delta^{18}O_{sw}$ representing fresher waters, which we interpret as a more intense monsoon discharge. This record of monsoon intensity displays a complex trend of stronger monsoons earlier in the glacial period, with intensity steadily decreasing from 42 to 37 ka. Several millennial-scale fluctuations are visible, such as elevated monsoonal strength at 46-52 ka, a peak at 42 ka, and a sharp low at 31 ka.

The planktic $\delta^{13}C$, also presented with a locally weighted smoothing curve, shows an increase from approximately 0.31‰ to 0.75‰ throughout the record (Figure 16). The peaks during the interval from 46-52 ka and at 42 ka match those of the $\delta^{18}O_{sw}$ record. However, the peak at 37 ka and low at 34 ka do not appear to correspond to monsoon freshening events. Planktic $\delta^{13}C$ can be influenced by many factors, including productivity and air-sea gas

exchange, and is often left without interpretation; but the matching appearance of the δ^{13}C and δ^{18}O records merits speculation.

The benthic δ^{18}O displays a positive trend from 3.2‰ to 3.5‰ from 55 ka to 21 ka (Figure 16). Part of this trend may be attributed to the accumulating ice sheets during the last glacial period. Superimposed on this trend are several excursions of lighter δ^{18}O, present at approximately 54, 44, 41, and 37 ka. The $\delta^{18}O_{ben}$ content in these excursions range from 3.1‰ to 2.8‰; between these excursions, the δ^{18}O returns to a base level of 3.5–3.6‰. The magnitude of these excursions exceeds those expected from global ice volume changes reflected in the sea-level records from Siddall et al. (2003). These excursions are opposite in phase to those of the monsoon freshening events in the $\delta^{18}O_{sw}$ record.

The benthic δ^{13}C is dominated by a strongly positive trend from approximately -.057‰ to -0.12‰ (Figure 16). Again, excursions punctuate the record at approximately 54, 44, 41, and 37 ka, aligning with those in the $\delta^{18}O_{ben}$ record. Additional peaks at 50 and 28 ka are more extreme than those in the benthic δ^{18}O at the same time. As discussed below, these positive excursions may represent intrusion of a water mass with less remineralized organic carbon. The general trend towards positive $\delta^{13}C_{ben}$ would then reflect increasing ventilation of the subsurface water mass over time.
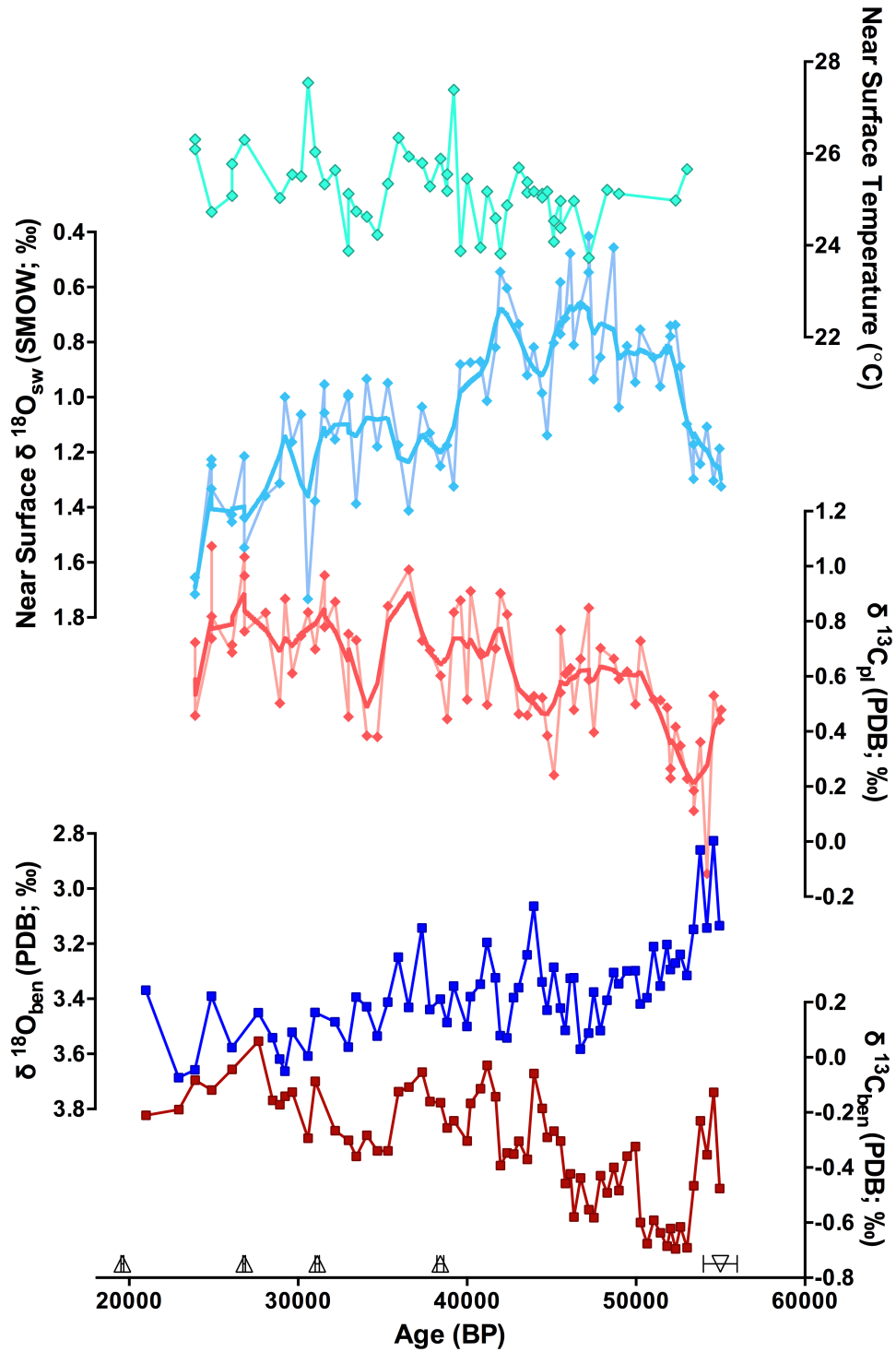
Figure 16: Core NGHP-01-19B near surface seawater temperatures, δ¹⁸O_{sw}, planktic δ¹³C, benthic δ¹⁸O, and benthic δ¹³C plotted with age, and age control points are included with error bars. Planktic-derived values are shown with a lowess curve. While each data set has its own trend, some fluctuations are present in multiple records.
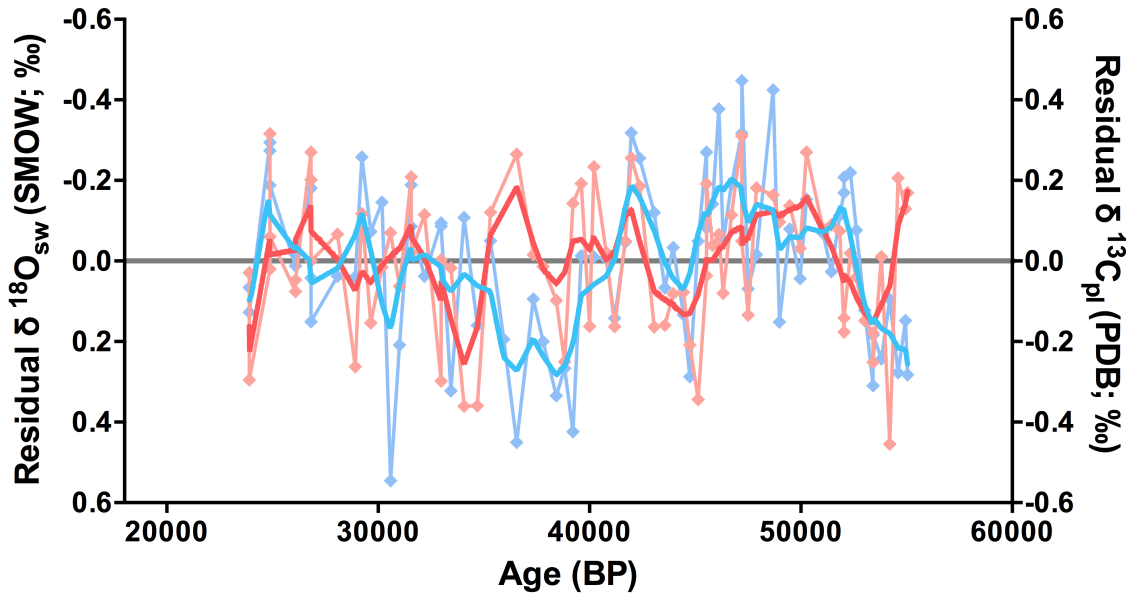
Figure 17: Residual δ¹⁸O_{sw} (blue) with residual δ¹³C_{pl} (red) versus age, and respective lowess curves highlighting the similarity of the fluctuations present.
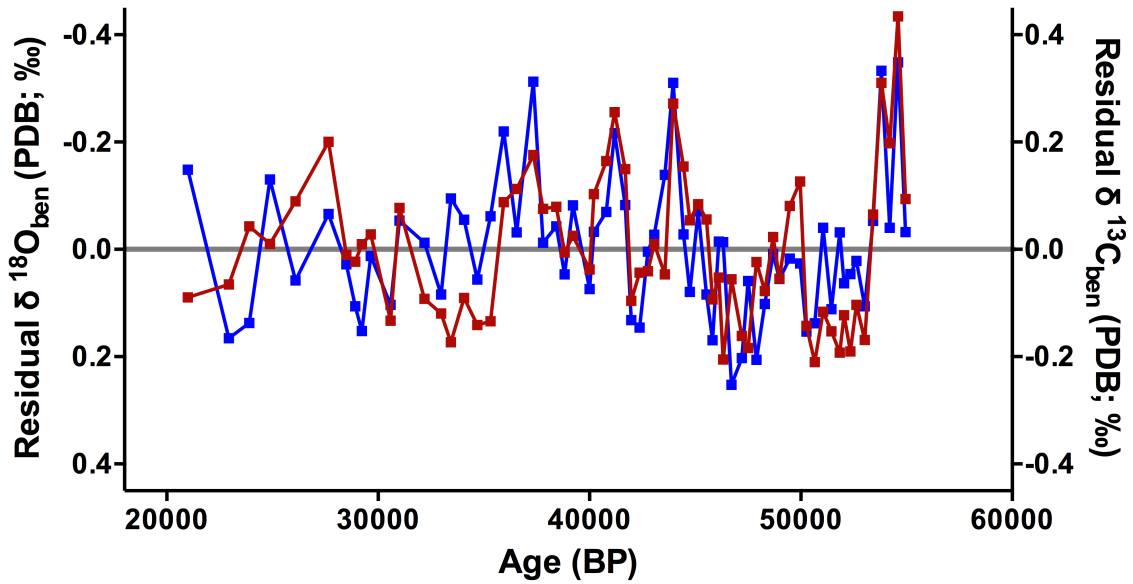
Figure 18: Residual δ¹⁸O_{ben} (blue) with residual δ¹³C_{ben} (red), which vary in sync with each other.
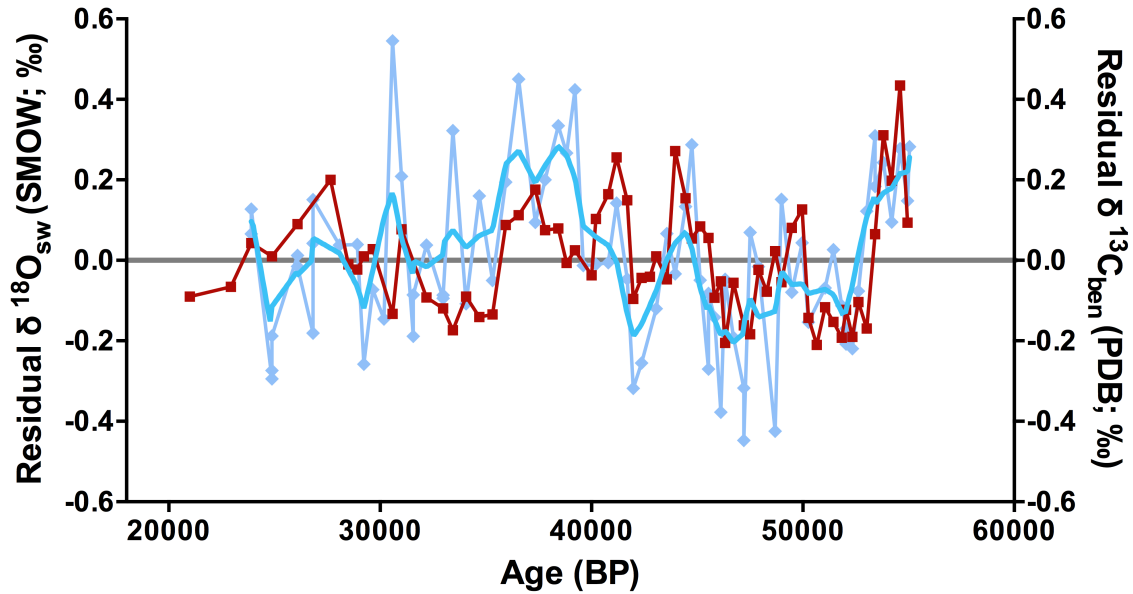
Figure 19: Residual δ^{18}O$_{sw}$ (blue) and residual δ^{13}C$_{ben}$ (red). In this figure, the axis for planktic δ^{18}O is not reversed; a more negative signal (indicating a stronger monsoon) matches the negative orientation of the benthic fluctuations.
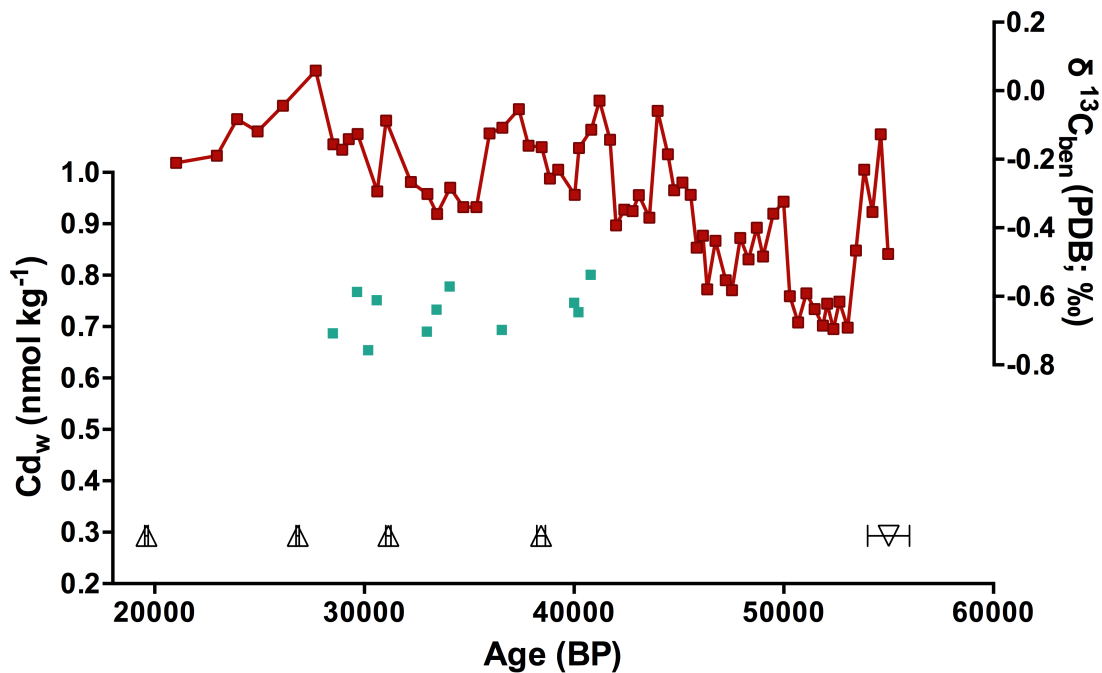
Figure 20: Benthic nutrient tracers for Core NGHP-01-19B. Cd$_w$ (green) from *H. elegans* and δ^{13}C$_{ben}$ of *Cibicidoides* spp. (red). Age control points included.

Discussion

Lead-Lag Relationships

Sea surface temperature is correlated to $\delta^{18}O_{sw}$, but this is expected because $\delta^{18}O_{sw}$ is derived from the temperature record. More positive planktic $\delta^{18}O_{sw}$ is indicative of a weaker monsoon, with positive excursions representing saltier water due to lessened rainfall. The positive correlation indicates that decreases in precipitation are associated with warmings in the Mahanadi Basin. The lack of monsoon discharge from land may have caused sea surface temperatures to rise. Higher SSTs were also found in the equatorial eastern Indian Ocean during Heinrich events (Mohtadi et al., 2014), suggesting this is not merely a local phenomenon. However, the lower resolution of the SST record means that this relationship is not statistically significant.

The planktic $\delta^{13}C$ roughly corresponds to the $\delta^{18}O_{sw}$ (Figure 17). When $\delta^{18}O_{sw}$ and $\delta^{13}C$ are each detrended from a quadratic fit (Table 3), lagged correlation analysis yields a correlation coefficient (r) of -0.22 at a near-zero lag. This value is below the .36 r value which represents the $p < 0.05$ significance for the 19 B records, derived using the method of Davis to measure joint probabilities (Davis, 1976). However, as is the case for all of the following relationships, the correlation is much higher in the earlier part of the record, from 40 to 55 kyr.

The matching planktic $\delta^{13}C$ and $\delta^{18}O_{sw}$ signals may indicate that during periods of more intense monsoons, local productivity increased, causing greater fractionation of the surface ^{13}C. (There exists a connection between monsoons and productivity, e.g., Guptha et al., 1997). However, wind mixing at the tropics will lower the $\delta^{13}C$ of carbon in surface waters; so perhaps this more positive signal during strong monsoons represents less air-sea gas exchange when the

surface ocean is more highly stratified. There does not appear to be a strong influence from terrestrial carbon, which has a much lower (more negative) $\delta^{13}C$ signature (Crowley, 1995).

Multiple productivity proxies have been analyzed at site 19 B at an approximately 1000-year temporal resolution over the last 110 kyr (Phillips et al., 2014). Mass accumulation rate of biogenic silica indicates that siliceous productivity was generally constant for the time interval from 55-24 ka at this core location. The mass accumulation rate of $CaCO_3$ shows some minor fluctuations during this interval, where higher productivity roughly corresponds to weaker monsoons. However, the planktic $\delta^{13}C$ record peaks during stronger monsoons. Therefore, it seems likely that wind mixing was a stronger influence than biology on fractionating the planktic $\delta^{13}C$.

As shown in Figure 18, the benthic $\delta^{13}C$ and $\delta^{18}O$ residuals covary as well. High $\delta^{13}C_{ben}$ values are associated with lower $\delta^{18}O_{ben}$, with a near-zero time lag correlation coefficient (r) of -0.60 (which is above the significance level of 0.36). Again, this correlation is strongest (r = .86) in the earlier part of the record, before 40 kya. The closely linked $\delta^{13}C$ and $\delta^{18}O$ of the benthic foraminifera suggests that the fluctuations are indicative of variations in the influence of a water mass, rather than changes in local factors. While it is possible that the presence or absence of a freshwater lens could impact the deepening and shoaling of isopycnals, that is not likely to be a dominant affect at this depth (1422 m) and distance from shore (~40 km during the last glacial period) (Phillips et al., 2014).

One possible bias in benthic $\delta^{13}C$ is that high productivity in surface waters can cause changes in benthic $\delta^{13}C$ which are not related to variations in water mass source (Mackensen et al., 1993). To check whether benthic $\delta^{13}C$ is influenced by the surface waters at this site, the planktic and benthic $\delta^{13}C$ residuals were tested for any lagged correlation. Their correlation

coefficient is 0.04 at a zero-time lag, and does not reach a significant value in lagged correlation analysis. The conclusion is that there is no consistent match observed between the planktic and benthic $\delta^{13}C$. We keep in mind, however, that the $\delta^{13}C_{pl}$ may not be a good indicator of surface productivity.

The stable isotope content of the benthic foraminifera also vary in sync with the planktic $\delta^{18}O_{sw}$. As shown in Figure 19, lower planktic $\delta^{18}O_{sw}$ values are associated with lower benthic $\delta^{13}C$, which also corresponds to higher benthic $\delta^{18}O$ (Figure 18). The correlation coefficient between $\delta^{13}C_{ben}$ and $\delta^{18}O_{sw}$ is 0.33 at a zero-time lag and 0.41 when surface properties lag subsurface properties by 380 years. Likewise, a lagged correlation analysis between $\delta^{18}O_{sw}$ and $\delta^{18}O_{ben}$ reveals a correlation coefficient of -0.43 between 140 years of planktic lead to 480 years of planktic lag. These are both considered to be above the significance level of $r = 0.36$. Again, the relationship is much stronger in the earlier part of the record, with similar lags.

Using the benthic $\delta^{13}C$ as a water mass tracer, the simplest interpretation would be that intrusions of high $\delta^{13}C$ resulted from increased ventilation of the intermediate-depth waters bathing the 19 B site. The more quickly circulating water mass had less time for remineralization of the biologically-fractionated, organic-bound ^{12}C, leaving a higher $\delta^{13}C$ signal. These peaks in $\delta^{13}C$, representing increased ventilation of the intermediate water, are in opposite phase with strong monsoons. (That is, increases in ventilation occur along with weaker monsoons.) The correlation does not hold in the opposite direction; the monsoon unambiguously lagged the changes in circulation. The implications of this are addressed in more detail below.

Very few Cd_w data were generated in this study. There is no relationship between higher Cd_w and lower $\delta^{13}C_{ben}$ values (Figure 20). Thus we do not suggest that variability within the cadmium data is representative of the changing water mass state. Rather, the range of values

constrains the nutrient content of the water mass independently from the benthic $\delta^{13}C$. The

cadmium can then be paired with the $\delta^{13}C_{ben}$ data to create a nutrient signature of the water mass

as a whole from 40-30 ka.
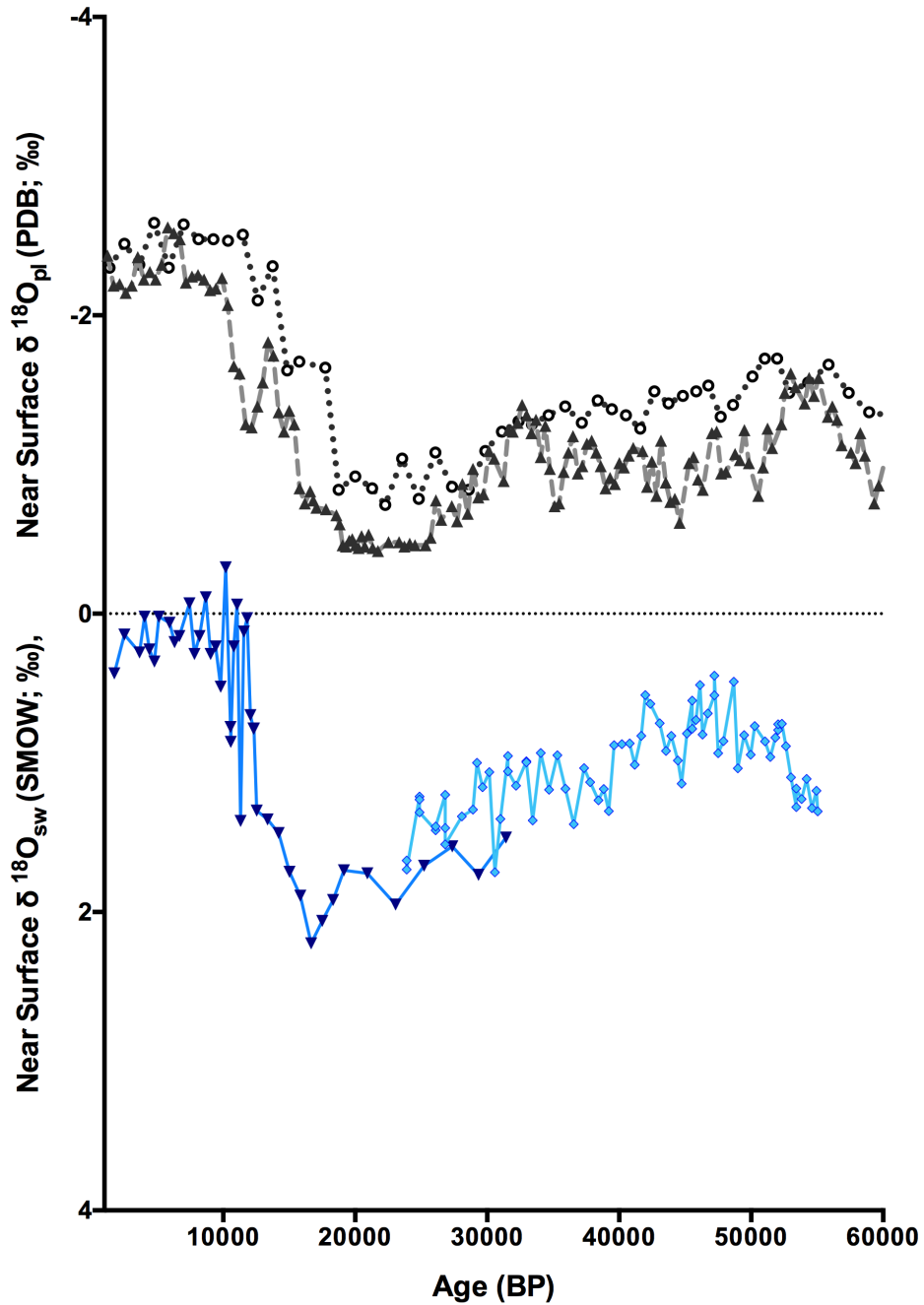
Figure 22: Planktic *G. ruber* δ^{18}O near the Bay of Bengal. Blue diamonds are from this study; blue upside down triangles are also Core 19 B (Shulenberg 2012); both are temperature-corrected and thus converted into δ^{18}O$_{sw}$. Open circles are from Bolton (2013) and triangles from Ahmad (2012); these two study sites are near the equator and so may record less local freshening. Both are not temperature corrected (δ^{18}O of calcite).

Variability in the Intensity of the Indian Monsoon

The overall trend of the δ^{18}O of *G. ruber* demonstrates a decreasing intensity of the monsoon throughout the time period from 55-24 ka. This conclusion is in good agreement with other reconstructions using *G. ruber* δ^{18}O near the Bay of Bengal (Figure 21). The 19 B δ^{18}O$_{sw}$ record in Figure 21 is shown with local records, including earlier work done on the same core (Schulenberg, 2011, also temperature-corrected). The other two records shown (Ahmad et al., 2012; Bolton et al., 2013), dated by radiocarbon and SPECMAP benthic oxygen isotopes, are both from equatorial locations near the 90-East Ridge. Both are records of δ^{18}O$_{pl}$ uncorrected for temperature or ice volume. As there is uncertainty in each of the age models, it is expected that the exact timing of any events recorded in the three cores would be different. There is no clear relationship between the millennial-scale events present in 19 B and the variability present in the equatorial records. This may be because the 19 B core site is within the northwestern Bay of Bengal, considerably nearer to land, and may record more local freshening than these records.

Several fluctuations are visible in the 19 B δ^{18}O$_{sw}$ record, such as elevated monsoonal strength at 46-52 ka, a peak at 42 ka, and a low at 31 ka. These excursions align with regional monsoon records seen in East Asian speleothems, which in turn align with the Greenland ice core record (Wang et al., 2001; Figure 22). While there are criticisms that part of the speleothem record is dictated by changes in the δ^{18}O of precipitation source waters rather than purely monsoonal intensity (e.g. Clemens et al., 2010), synchronicity with Greenland was also found in a monsoon record from a Bay of Bengal sediment core (core SO93-126KL, Kudrass et al., 2001; Figure 22). However, the match between SO93-126KL and the Greenland ice core is not unexpected due to the fact that the sediment record was tuned to the Greenland record. In contrast, the age model for 19 B was generated using radiocarbon to 38.4 ka BP, and then the

benthic record was tuned to Lisiecki and Raymo (2005) at 55 ka. This leaves the exact timing of events offset from the other records.

Since core SO93-126KL is located in a hydrographically similar location to 19 B, both records should reveal similar monsoon signals. However, the quality of the excursions are not identical: the SO93-126KL record, like the East Asian speleothem, displays more variability and sharper changes, while the 19 B record is shows gradual increases and decreases. Much of this disagreement in character is doubtless due to aliasing of the finer-scale variability in the 19 B sediment core, or possibly smoothing by bioturbation. On the other hand, this may indicate that the Indian Monsoon was not affected by climate change in the exact way that the East Asian monsoon was.

When the 19 B $\delta^{18}O_{sw}$ record is compared to the polar ice records (Figure 22), the events present broadly suggest a more intense monsoon during warm periods over Greenland and cold periods over Antarctica, in agreement with previous records (Kudrass et al., 2001; Schulz et al., 1998; Wang et al., 2001). However, the claim of synchronous changes between monsoon intensity and Greenland temperatures is not supported by the 19 B record at a finer scale. For example, the peak at 43 ka is a gradual peak in the 19 B record, but occurs in a series of sharp changes in the GISP2 record and speleothem record. Furthermore, the pronounced GISP2 warm event at 37 ka corresponds to a series of events in the speleothem record, but is barely present in the 19 B $\delta^{18}O_{sw}$ record. (Interestingly, there is a corresponding response in planktic $\delta^{13}C$ despite little change in monsoon intensity as recorded in $\delta^{18}O_{sw}$ (Figures 17, 18); this may indicate a decoupling of wind mixing and freshwater-controlled stratification.) In these earlier events, the 19 B record is more similar to the reversed Antarctic ice record than the Greenland record. One event, the low in $\delta^{18}O_{sw}$ at 31 ka, does appear to correspond to an event affecting only Greenland

climate. This implies that the changes in the monsoon are somehow linked or associated with Northern Hemisphere climate, but are not necessarily synchronous.

Thus, the relationship between 19 B and ice core records seen in Figure 22 supports a partial influence of Greenland climate during major climate events. However, it does not support the synchronicity suggested by Kudrass et al. (2001) and Wang et al. (2001). Instead, it just as strongly suggests that Southern Hemisphere climate exerted an influence on monsoon intensity during the last glacial period. Thus, the 19 B record is consistent with the Rohling et al. (2009) hypothesis that the Indian monsoon experienced a Southern Hemisphere influence during the last glacial period. However, a shift to a Northern Hemisphere influence must have begun as early as the 31 ka event seen in the 19 B record. This emphasizes how the millennial scale events seen in the polar ice records were global in nature, and suggests that the monsoon may be influenced by both hemispheres during glacial periods (Caley et al., 2013).

The short length of this $\delta^{18}O_{sw}$ record (31,000 years) precludes a rigorous analysis of orbital forcing. When the record is visually compared to Mid-June insolation at 30°N (Berger and Loutre, 1991), the signals are nearly in opposite phase (Figure 23). This is in opposition to the orbital insolation hypothesis (Ruddiman, 2006; Ziegler et al., 2010) which predicts that monsoon intensity would be concurrent with insolation changes. However, it may be the appearance of opposite phasing is merely due to the shorter frequency millennial-scale variability dominating the $\delta^{18}O_{sw}$ signal. Likewise, the 8 kyr lag suggested by Clemens and Prell (2003) is not evident either; instead, the lag between peaks is around 16 kyr. This would suggest that forcing factors internal to the climate system control monsoon intensity more strongly than insolation. However, a longer record would be needed to establish the genuine peaks and troughs of monsoon intensity.
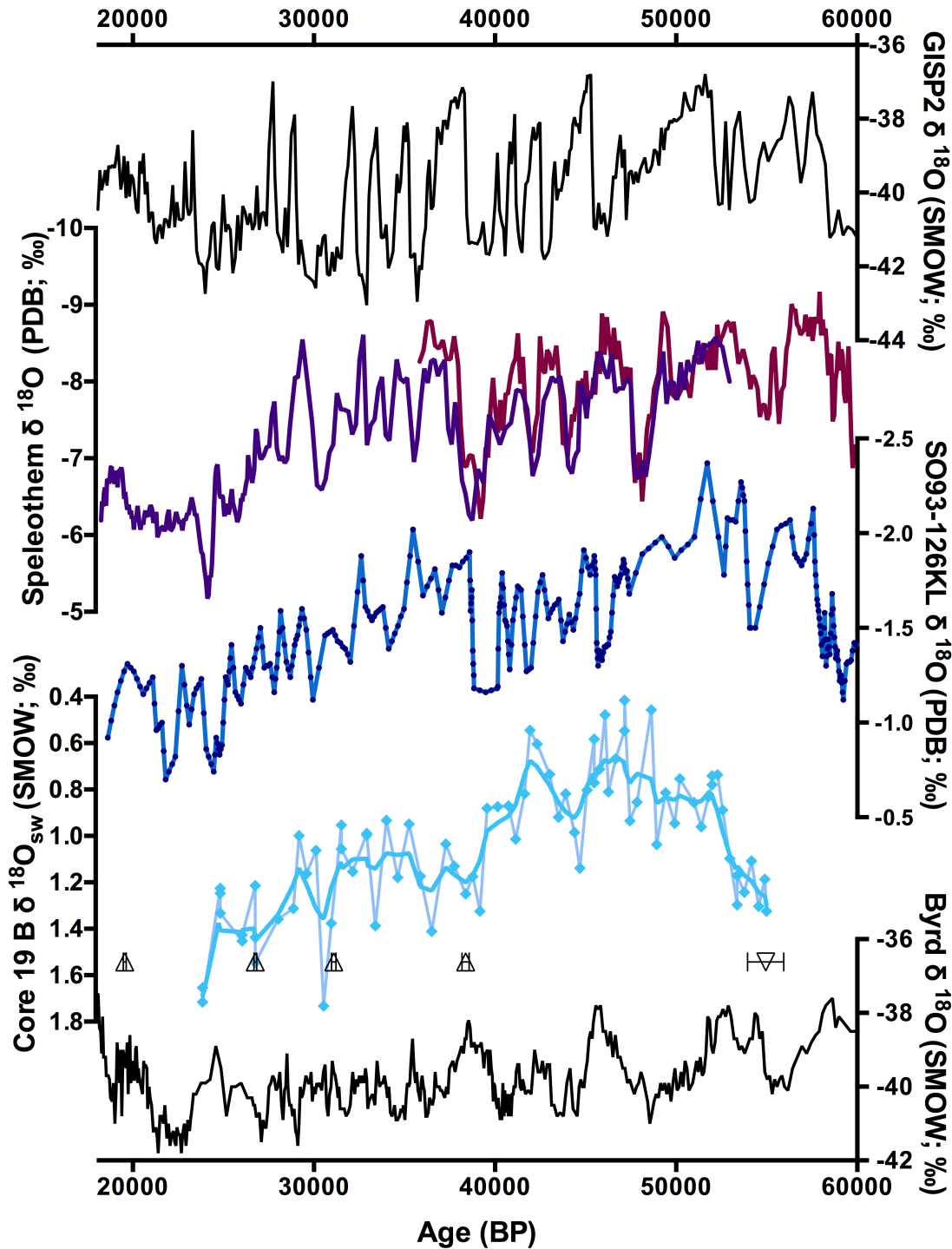
Figure 22: Core NGHP-01-19B near surface $\delta^{18}O_{sw}$ compared with nearby sediment core SO93-126KL (Kudrass 2001), speleothem records of the East Asian monsoon (Wang 2001), and ice cores from each hemisphere (Blunier and Brook 2001).
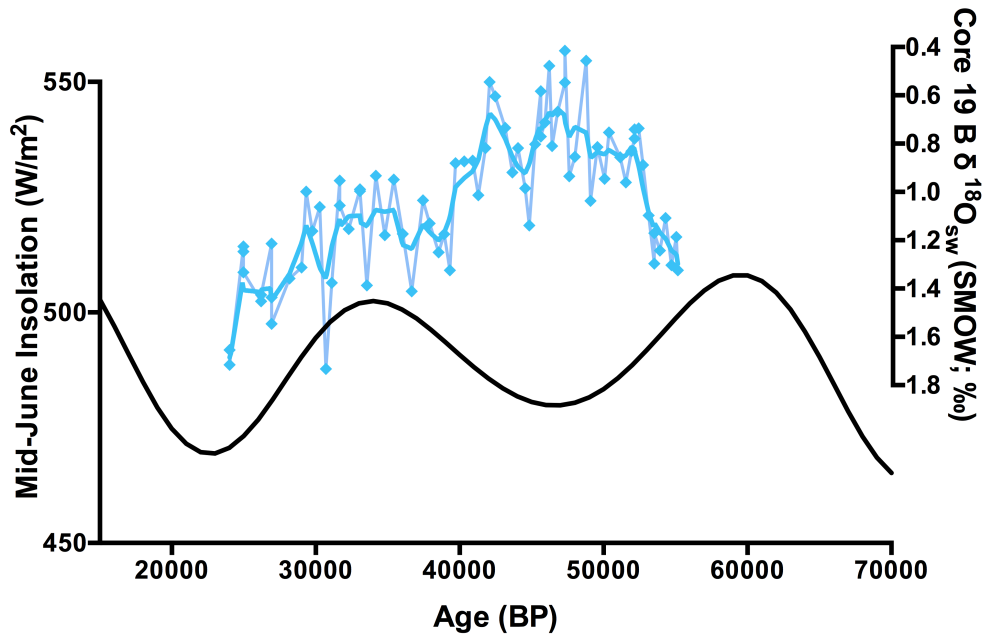
Figure 23: Core NGHP-01-19B near surface δ^{18}O$_{sw}$ compared with summer insolation at 30°N (Berger 1991). The monsoon data do not support direct insolation forcing.
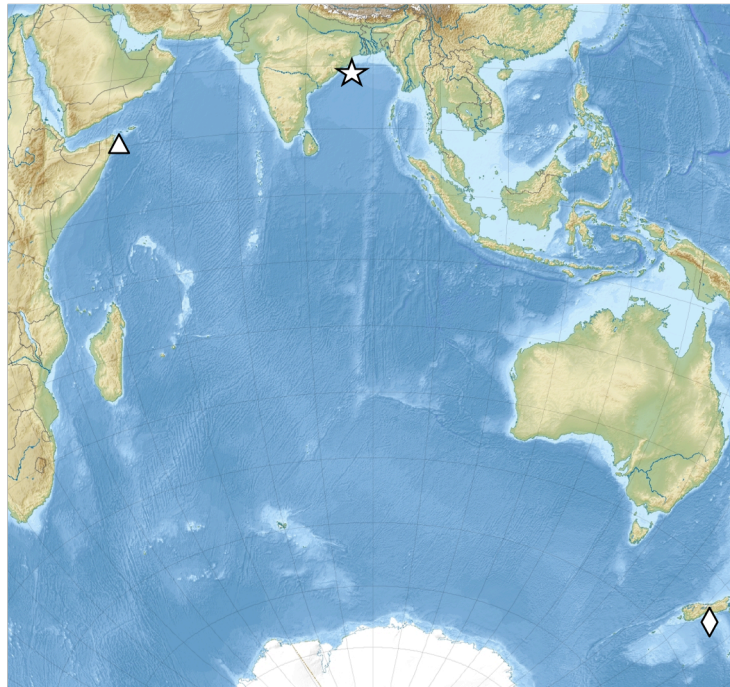
Figure 24: Map showing the location of the core sites where GAAIW may have reached during the last glacial period. The triangle is Core NIOP 905, 1580 m depth (Jung et al. 2009); the diamond is Core MD97-2120, 1210 m depth (Pahnke and Zahn 2005); the star is Core NGHP-01-19B, 1422 m depth (this study).
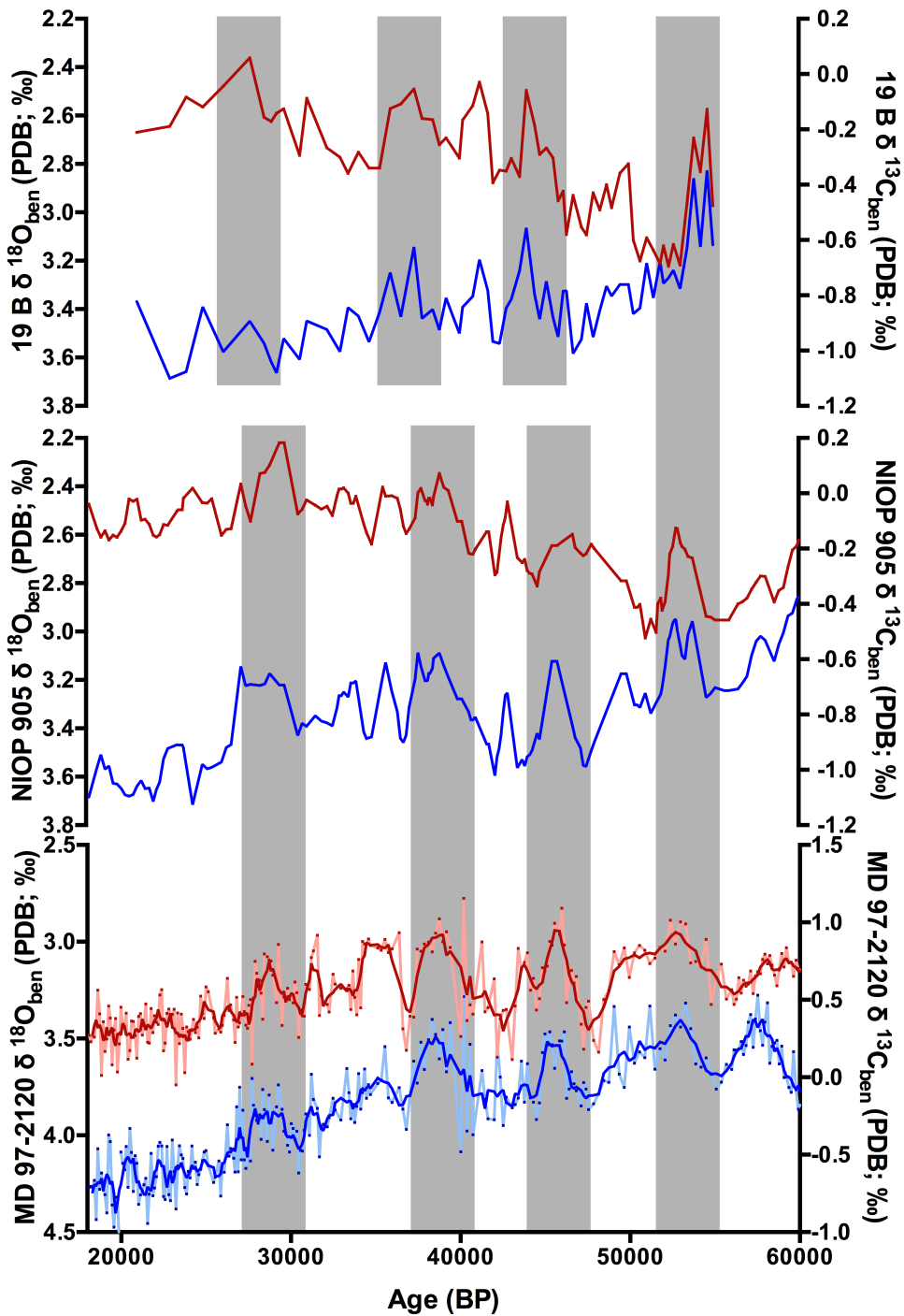
Figure 25: Benthic $\delta^{18}O_{ben}$ and $\delta^{13}C_{ben}$ data from the three cores: Core NGHP-01-19B (this study), Core NIOP 905 (Jung et al. 2009), and Core MD97-2120 (Pahnke and Zahn 2005), shown with a five-point local average; the locations of all are shown in Figure 24. All are from *Cibicidoides* spp. Grey bars highlight periods of invigorated AAIW.

Variability of Intermediate-depth Water Mass

The benthic stable isotope records from site 19 B show the presence of a water mass with a $\delta^{18}O$ signature of about 3.5‰, periodically pierced by excursions of lower-$\delta^{18}O$, high-$\delta^{13}C$ water accompanying decreases in monsoon intensity. A similar structure of lower-$\delta^{18}O$, high-$\delta^{13}C$ spikes in benthic intermediate water, also in reverse phase with stronger monsoon signals, was found in Core NIOP 905 off the coast of Somalia (Jung et al., 2009). These values are nearly identical to those at site 19 B (Figure 25). Following the lead of Pahnke and Zahn (2005), Jung et al. suggest that the high $\delta^{13}C$ in intermediate depth waters (1580 m) was due to intermittent invigorations of Glacial Antarctic Intermediate Water (GAAIW). In this model, the variability of about 0.5‰ in the $\delta^{18}O_c$ is caused by warming at the site of water mass formation; and the variability in the $\delta^{13}C$ is caused by the age of the water mass varying with circulation speed. It is reasonable to suppose that the intermediate-depth water mass affecting the NIOP 905 site in the Arabian Sea during the last glacial period also reached our core site in the Bay of Bengal. Although AAIW does not reach this far north in the Bay during modern times, the studies mentioned previously indicate it may have during the last glacial maximum (Boyle et al., 1995; Kallel et al., 1988).

However, other possibilities to explain the variations in $\delta^{13}C_{ben}$ and $\delta^{18}O_{ben}$ are considered below. In modern times, the water present at the 19 B core site is a mixture of Red Sea Water (RSW) from the Arabian Sea and south-returning Indian Deep Water (IDW). Changes in the influence of either of these water masses may have affected the water at the 19 B core site during the last glacial period. Other potential water masses that could have been present at 1400 m depth might include Indonesian Intermediate Water (IIW), if it were significantly less buoyant than in the modern ocean. It is also possible that during the last glacial, increased evaporation in

the Indian Ocean led to the sinking of subtropical convergence water (Boyle et al., 1995; Kallel et al., 1988).

Changes in the water mass at our core site could be a reflection of the changing influence of Indian Deep water, which is very aged south-returning NADW. NADW formation is known to have fluctuated in strength throughout the last glacial, at times forming intermediate water (GNAIW) rather than deep (Curry and Oppo, 2005; Duplessy et al., 1988; Oppo and Lehman, 1993). While GNAIW isn't thought to extend to the global ocean, its formation may have been associated with a slowing of the entire global overturning circulation. However, this scenario of a slackening of circulation would result in lowering δ^{13}C levels without a change in δ^{18}O content, and so would not fully explain the record present at site 19 B. Furthermore, δ^{13}C measured in cores 3306 – 2855 m depth in the equatorial Bay of Bengal, which must have been typical of Indian Deep Water throughout the last glacial, give no indication of the steep changes in δ^{13}C as seen in the 19 B record (Ahmad et al., 2012; Raza et al., 2014).

In order for glacial IIW or subtropical convergence water to have reached the 19 B site, it would have been necessary for them to sink 500 and 1000 m deeper during the last glacial than they do today, respectively. Being tropical water masses, the only way for either of them to gain density would be for evaporation to concentrate salinity in their surface waters. In this case, they would both have been warm, very salty water masses that were recently near the surface. Their high salinity may have caused one (or both) of these water masses to enter the Bay of Bengal at depth, carrying higher δ^{13}C due to more recently being at the surface (See Figure 7 for δ^{13}C distribution the modern in Indian ocean). However, the high δ^{18}O$_{ben}$ of around 3.0‰ indicates that the water present at 19 B must have been of a much colder origin (Epstein et al., 1953; Railsback et al., 1989; Rohling and Bigg, 1998), so surface water can not be the primary water

mass responsible for the high $\delta^{13}C$. Furthermore, there is no current evidence that supports the idea that the IIW or subtropics gained such a large amount of salinity during the last glacial period.

A similar reasoning applies to RSW. In the modern ocean, RSW extends to about 1400 m depth (Talley et al., 2011), but the shallow sill of the Red Sea means that its waters were more saline during the sea level lows of the last glacial period (Siddall et al., 2003). This, in addition to the lower eustatic sea level shoaling our core site, may have allowed RSW to reach our modern core depth of 1422 m. Changes in sea level could have caused varying volumes of RSW to enter the Arabian Sea and then the Bay of Bengal. RSW in modern times is highly depleted in $\delta^{13}C$ (Schlitzer, 2014; Figure 7), with values ranging from 0 to -0.5‰. Assuming this held true during the last glacial period, the higher values of $\delta^{13}C$ (around 0‰) associated with lighter $\delta^{18}O$ in the benthic record at site 19 B could potentially be explained by RSW. This explanation requires that the ambient water mass present at site 19 B was even more nutrient rich than RSW, as could be the case if the primary water mass at the core site was aged, south-returning IDW. However, the very heavy $\delta^{18}O$ values indicate that most of the water at the 19 B core site was derived from a much colder source than RSW.

The average oxygen signature of planktic foraminifera in the Red Sea during the period from 55 to 24 ka is 0.7‰ (with a range from 2.5 to -1‰) (Siddall et al., 2003). Converting this to a corresponding *Cibicidoides* $\delta^{18}O_c$ using a range of temperatures from 20-30°C (Kim and O'Neil, 1997; Mulitza et al., 2003) results in a typical $\delta^{18}O_c$ of 1.2 ‰ (but with a potential range from -0.6 to 2.5‰). This means that the carbonate forming in these outflow waters would be over 2‰ lighter than the $\delta^{18}O_c$ seen in the benthic record at site 19 B. If this RSW reached our core site at intermittent times through the last glacial period, it could be indicated by the

excursions toward lighter $\delta^{18}O$ in the benthic 19 B record. However, the fact that the benthic $\delta^{18}O$ is much higher (around 3.5‰) during most of the record indicates that glacial RSW was not the primary water mass at our core site, and could only be present in minor amounts even during the most extreme lighter-$\delta^{18}O$, high-$\delta^{13}C$ events.

While glacial RSW was not the primary water mass at site 19 B, it could have had some influence on the stable isotope records. The phase of pulses of RSW and GAAIW would be concurrent according to high-resolution salinity records in the Red Sea, which suggest a heightened sea level coincident with warm events in the Antarctic throughout the last glacial (Siddall et al., 2003). In the modern ocean, RSW and GAAIW have the same density range, allowing mixing (Talley et al., 2011). Therefore, it is possible that some combination of both water masses was present at our core site during times of lighter $\delta^{18}O$ and high $\delta^{13}C_{ben}$.

Therefore, the GAAIW hypothesis (as in Jung et al., 2009) remains the simplest explanation for the benthic variability found in core 19 B. This is in agreement with previous evidence from the northern Indian Ocean: stable isotope profiles from the last glacial maximum show a sharp distinction between the $\delta^{18}O_c$ of intermediate water and deep water (>2000 m) (Kallel et al., 1988), suggesting strong stratification between intermediate and deep waters and implicating different sources. Likewise, a distinction in the $\delta^{13}C$ signatures indicates that the intermediate water is younger than the deep water (Kallel et al., 1988). This would be the case if GAAIW were present in the Bay of Bengal.

Scrutiny of validity of the GAAIW hypothesis

To check whether the high-$\delta^{13}C$ water mass could potentially be GAAIW, multiple parameters are examined. A similar pattern of high-$\delta^{13}C$ signals during lower-$\delta^{18}O$ events is found in benthic signals from a location in the core of GAAIW south of New Zealand (Pahnke

and Zahn, 2005), and also in the intermediate waters of the Arabian Sea during the last glacial period (Jung et al., 2009) (See Figure 24, Figure 25). If these are the same water mass, their stable isotope and nutrient content should be in agreement.

The oxygen stable isotope content of a water mass is set by the evaporation/precipitation environment when it is at the surface. Once subducted, the $\delta^{18}O$ remains unchanged from its original imprint, as $\delta^{18}O$ is a conservative property. The temperature of the water will have some further impact on $\delta^{18}O_c$ formed within it; but temperature is mostly conservative as well.

Similarly, the carbon stable isotope content of a water mass is determined by the air-sea gas exchange at the formation site, which can vary with: temperature; ice cover; wind speeds; residence time of the surface water before being subducted. Additionally, carbon is fractionated by photosynthesizers (Kroopnick, 1985; Lynch-Stieglitz et al., 1994). Once set by these factors, the $\delta^{13}C$ will change predictably in transit as biological respiration releases ^{12}C back into the water column. Thus, $\delta^{13}C$ is an indicator of a water mass's age, if the original $\delta^{13}C$ of that water mass is known (Lynch-Stieglitz et al., 1994).

Modern AAIW is marked by different water-mass signatures in the Pacific than the Atlantic, due to differences in these water masses' formation; Atlantic AAIW is formed from altered Pacific AAIW (Talley et al., 2011). The AAIW that enters the Indian Ocean in modern times is thought to originate in the Atlantic, although there may be some contribution from locally-sourced Southeast Indian Subantarctic Mode Water (SEISAMW) (Talley et al., 2011). Thus, water mass tracers would be expected to reflect Atlantic-formed GAAIW rather than Pacific-formed GAAIW. However, lack of a high-resolution Atlantic GAAIW for our time window compels us to use the Pahnke and Zahn record from Pacific GAAIW for comparison, despite the known differences in sources.

The newly-formed Pacific GAAIW had a $\delta^{18}O_c$ signature of ~3.4‰ during periods of high-$\delta^{13}C$ as recorded in Core MD97-2120 south of New Zealand (Pahnke and Zahn, 2005) (See Figure 25). This water mass, presumably somewhat altered in the Atlantic as well as aged, was detected in off the coast of Somalia in NIOP 905 (Jung et al., 2009), where the $\delta^{18}O_c$ averaged ~3.0‰ during high-$\delta^{13}C$ events. Similarly, periods of high-$\delta^{13}C$ in the 19 B record also correspond to a $\delta^{18}O_c$ of ~3.0‰. The differences in the timing of these events between the 19 B and NIOP 905 is likely due to age model uncertainty.

The periodic high peaks in the $\delta^{13}C$ values present in newly-formed Pacific GAAIW (Core MD97-2120) have a high $\delta^{13}C$ signature near 1.0‰. Peaks in the Somalian coast core (NIOP 905) and the 19 B record are between 0.1‰ and -0.05‰. These low values at both of the Northern Indian Ocean sites would be expected if GAAIW traversed from another ocean basin, as aging a water mass lowers its $\delta^{13}C$ compared to the source. The slightly higher averaged $\delta^{13}C$ in the Somalian coast site suggests that water reaching Somalia is younger than water reaching site 19 B, which is expected given that the Somalian coast is adjacent to a western boundary current. This suggests that water mass entered from the western side of the Indian Ocean.

Cadmium data and the GAAIW hypothesis

The final parameter which can test the GAAIW hypothesis is seawater cadmium concentrations. Cd_w can be paired with $\delta^{13}C$ values to evaluate the nutrient signature of a water mass. In the ocean, $Cd_w/\delta^{13}C$ values change predictably as a water mass ages and its biological matter is remineralized according to the Redfield ratio (Lynch-Stieglitz et al., 1996). When plotted in Cd_w and $\delta^{13}C$ parameter space, the water mass moves in a straight line as it ages (Lynch-Stieglitz et al., 1996; Oppo and Horowitz, 2000).
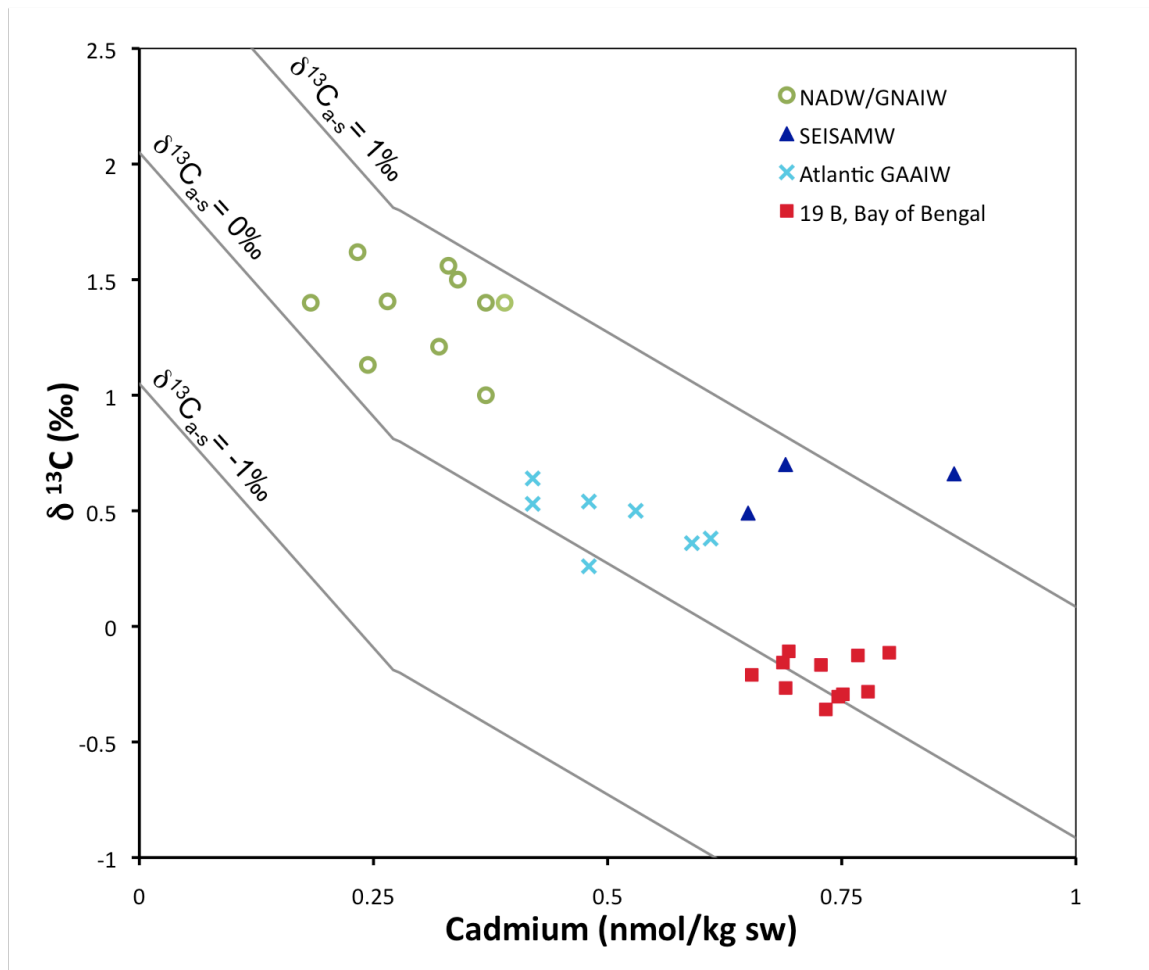
Figure 26: Cd$_w$ and δ^{13}C$_{ben}$ data from multiple locations during the last glacial period. Green circles represent North Atlantic Deep Water during the last glacial maximum (aka, GNAIW); data compiled in Marchietto et al. 2006. Dark blue triangles are values from a core from south of Australia which is thought to represent subducted Southeast Indian Sub-Antarctic Mode Water (Lynch-Stieglitz et al., 1996). Light Blue crosses are from the Brazilian margin, which represent Atlantic GAAIW (Makou et al., 2010). Red squares are Core 19 B data (this study). Figure after Lynch-Stieglitz et al. 1996, Oppo and Horowitz 2000.

The paired Cd_w and $\delta^{13}C$ values are shown in Figure 26. The position on the lower right side of the diagram shows that the water at site 19 B is, in general, fairly aged. Because cadmium was only measured in a portion of the core, this represents the water mass present from about 40 to 30 ka (Figure 20). However, most of the published Cd_w data which provides a global context for our dataset was measured at the Last Glacial Maximum, which occurred around 20 ka.

AAIW in the modern Indian Ocean is thought to be sourced from Atlantic-formed AAIW (Talley et al., 2011). However, it is possible that during the last glacial period, AAIW was sourced or influenced by the more locally-formed Southeast Indian Subantarctic Mode Water (SEISAMW). Cadmium and $\delta^{13}C$ levels have been measured at the LGM in both Atlantic AAIW and Indian Ocean SAMW (Lynch-Stieglitz et al., 1996; Makou et al., 2010; Figure 26).

The $Cd/\delta^{13}C$ values for newly-formed Atlantic GAAIW come from a depth transect study off the Brazilian margin (Makou et al., 2010). These fall along the same trajectory as the nutrient signature in core 19 B. This supports the interpretation that the benthic water present at site 19 B was aged GAAIW for the period of 40 to 30 ka.

In contrast, benthic data from the Pacific Ocean near Australia (1042-1650 m) displays a much higher Cd relative to $\delta^{13}C$ (Lynch-Stieglitz et al., 1996). If this nutrient signature is characteristic of Southeast Indian Subantarctic Mode Water during the last glacial, this indicates that the water present at site 19 B is not sourced from SEISAMW.

For comparison, Glacial North Atlantic Water (GNAIW/GNADW) from the LGM is included on Figure 26 (Marchitto and Broecker, 2006, References therein). Its nutrient signature near formation is offset from both the Atlantic GAAIW and the core 19 B values, indicating a different water mass source. This suggests that aged NADW was not the source of the water present at core 19 B. We are wary of ruling out NADW as a source for the waters at site 19 B

based on the cadmium data alone, since NADW formation was unusual during the last glacial maximum, and paired cadmium and $\delta^{13}C$ have not been generated for the time period of 30-40 ka. However, as previously mentioned, continuous late glacial records of $\delta^{13}C$ at depths from 3306-28555 m from the equatorial Bay of Bengal also do not support aged NADW (IDW) as the source for the water at 19 B.

While there have not been Cd/$\delta^{13}C$ studies RSW during the last glacial period, its modern Cd_w content is much higher than the values found at site 19 B. Therefore, it is not probable that RSW was present at site 19 B from 40 to 30 ka. However it is not possible at this time to ascertain the influence of RSW on the nutrient content of our core site.

Therefore, this study is consistent with, but not definitive for, the identification of GAAIW in the Bay of Bengal, with a suggested source of aged Atlantic-formed GAAIW.

Planktic-Benthic Connection

The pattern of benthic $\delta^{13}C$ as a water mass tracer, as explained above, indicates periodic increases in the ventilation of the intermediate-depth water at the core site. If the $\delta^{18}O_{sw}$ reflects changes in monsoon intensity, then decreases in monsoon intensity occur with increases in intermediate water ventilation; and increases in monsoon intensity with decreases in ventilation. As stated above, the anti-phase relationship of the signals are not a perfectly synchronous "see-saw;" rather, the monsoon lags changes in subsurface water properties by about 380 years.

Benthic water mass signals preceding changes in planktic monsoon signals is in agreement with a previous study (Jung and Kroon, 2011). If the benthic signal is indeed indicative of GAAIW, and if GAAIW expansion is in pace with warming in Antarctica (Jung and Kroon, 2011; Pahnke and Zahn, 2005), then warm events in Antarctica are in opposite phase with a strong monsoon; and cold events in Antarctica slightly precede periods of monsoon

intensification. There is of course an additional lag from the formation of GAAIW to its arrival at our core site. For example, if we assign a delay of 1000 years for the transit of the subsurface water mass (as the nutrient content indicates the water is aged), this would imply a 1380 year lag between when changes in circulation are initiated and changes in the monsoon.

This leaves both interpretations open: that cooling in Antarctica forces a delayed strengthening of the monsoon system; or merely that cooling in Antarctica precedes warming in Greenland and the northern hemisphere, where atmospheric teleconnections force monsoon intensification. Our study implies is that there is some reoccurring change in the Southern Hemisphere which forces a change in the circulation of GAAIW, and that this event is later manifested in monsoon intensity. Thus we conclude there is likely an influence from both hemispheres on monsoon intensity, which emphasizes how the forcing of the Indian monsoon must be complex.

Conclusions

We have presented a record from 55 to 24 ka of Indian Monsoon intensity. There appear to be connections to both hemispheres in influencing millennial-scale variability in the intensity of the monsoon during the last glacial period. This is seen in the structure of surface $\delta^{18}O_{sw}$, $\delta^{13}C_{pl}$, and sea surface temperatures at our core site in the northwest Bay of Bengal.

The benthic $\delta^{13}C$ and $\delta^{18}O$ records from the same core are indicative of changing states of ventilation from a southern source of intermediate-depth water. Stable isotope content closely matches that found in an Arabian Sea sediment core from a similar depth (Jung et al., 2009), which was postulated to be due to the presence of Glacial Antarctic Intermediate Water. Cd_w analysis is consistent with the identification of this water mass as aged Glacial Antarctic Intermediate water. Millennial-scale events of high monsoon intensity are correlated with decreased intermediate-depth water ventilation, and conversely when monsoons are weak the study site experienced increased intermediate-depth ventilation. Lagged correlation analysis, as well as the fact that changes in circulation must be initiated some distance from the core site, indicates that events at depth precede those at the surface due to monsoon variability. This difference in timing is in support of a Southern Hemisphere influence over the Indian Monsoon during a portion of the last glacial period.

References

Adkins, J.F., McIntyre, K., Schrag, D.P., 2002. The Salinity, Temperature, and delta 18O of the Glacial Deep Ocean. Science 298, 1769–1773. doi:10.1126/science.1076252

Ahmad, S.M., Zheng, H., Raza, W., Zhou, B., Lone, M.A., Raza, T., Suseela, G., 2012. Glacial to Holocene changes in the surface and deep waters of the northeast Indian Ocean. Mar. Geol. 329-331, 16–23. doi:10.1016/j.margeo.2012.10.002

Altabet, M.A., Francois, R., Murray, D.W., Prell, W.L., 1995. Climate-related variations in denitrification in the Arabian Sea from sediment 15N/14N ratios. Nature 373, 506–509. doi:10.1038/373506a0

Altabet, M.A., Higginson, M.J., Murray, D.W., 2002. The effect of millennial-scale changes in Arabian Sea denitrification on atmospheric CO2. Nature 415, 159–162. doi:10.1038/415159a

Andreasen, D., 2008. UC Santa Cruz Stable Isotope Laboratory [WWW Document]. UCSC.edu. URL http://es.ucsc.edu/~silab/di.sampleCostTbl.php (accessed 12.1.13).

Barker, S., Diz, P., Vautravers, M.J., Pike, J., Knorr, G., Hall, I.R., Broecker, W.S., 2009. Interhemispheric Atlantic seesaw response during the last deglaciation. Nature 457, 1097–1102. doi:10.1038/nature07770

Berger, A., Loutre, M.F., 1991. Insolation values for the climate of the last 10 million of years. Quat. Sci. Rev. 10, 297–317.

Blunier, T., Brook, E.J., 2001. Timing of Millennial-Scale Climate Change in Antarctica and Greenland During the Last Glacial Period. Science 291, 109–112. doi:10.1126/science.291.5501.109

Bolton, C.T., Chang, L., Clemens, S.C., Kodama, K., Ikehara, M., Medina-Elizalde, M.,
Paterson, G.A., Roberts, A.P., Rohling, E.J., Yamamoto, Y., Zhao, X., 2013. A 500,000
year record of Indian summer monsoon dynamics recorded by eastern equatorial Indian
Ocean upper water-column structure. Quat. Sci. Rev. 77, 167–180.
doi:10.1016/j.quascirev.2013.07.031

Bond, G., Broecker, W., Johnsen, S., McManus, J., Labeyrie, L., Jouzel, J., Bonani, G., 1993.
Correlations between climate records from North Atlantic sediments and Greenland ice.
Nature 365, 143–147. doi:10.1038/365143a0

Böning, P., Bard, E., 2009. Millennial/centennial-scale thermocline ventilation changes in the
Indian Ocean as reflected by aragonite preservation and geochemical variations in
Arabian Sea sediments. Geochim. Cosmochim. Acta 73, 6771–6788.
doi:10.1016/j.gca.2009.08.028

Boyle, E.A., Keigwin, L.D., 1985. Comparison of Atlantic and Pacific paleochemical records for
the last 215,000 years: changes in deep ocean circulation and chemical inventories. Earth
Planet. Sci. Lett. 76, 135–150. doi:10.1016/0012-821X(85)90154-2

Boyle, E.A., Labeyrie, L., Duplessly, J.-C., 1995. Calcitic foraminiferal data confirmed by
cadmium in aragonitic Hoeglundina: Application to the Last Glacial Maximum in the
northern Indian Ocean. Paleoceanography 10, 881–900. doi:10.1029/95PA01625

Boyle, E.A., Rosenthal, Y., 1996. Chemical hydrography of the South Atlantic during the Last
Glacial Maximum: Cd and δ13C, in: Wefer, G. (Ed.), The South Atlantic: Present and
Past Circulation. Springer-Verlag, Berlin, pp. 423–443.

Bryan, S.P., Marchitto, T.M., Lehman, S.J., 2010. The release of 14C-depleted carbon from the

deep ocean during the last deglaciation: Evidence from the Arabian Sea. Earth Planet.

Sci. Lett. 298, 244–254. doi:10.1016/j.epsl.2010.08.025

Cai, Y., An, Z., Cheng, H., Edwards, R.L., Kelly, M.J., Liu, W., Wang, X., Shen, C.-C., 2006.

High-resolution absolute-dated Indian Monsoon record between 53 and 36 ka from

Xiaobailong Cave, southwestern China. Geology 34, 621. doi:10.1130/G22567.1

Caley, T., Malaizé, B., Zaragosi, S., Rossignol, L., Bourget, J., Eynaud, F., Martinez, P.,

Giraudeau, J., Charlier, K., Ellouz-Zimmermann, N., 2011. New Arabian Sea records

help decipher orbital timing of Indo-Asian monsoon. Earth Planet. Sci. Lett. 308, 433–

444. doi:10.1016/j.epsl.2011.06.019

Caley, T., Zaragosi, S., Bourget, J., Martinez, P., Malaizé, B., Eynaud, F., Rossignol, L., Garlan,

T., Ellouz-Zimmermann, N., 2013. Southern Hemisphere imprint for Indo-Asian summer

monsoons during the last glacial period as revealed by Arabian Sea productivity records.

Biogeosciences 10, 7347–7359. doi:10.5194/bg-10-7347-2013

Cawthern, T., Johnson, J.E., Giosan, L., Flores, J.A., Rose, K., Solomon, E., 2014. A late

Miocene–Early Pliocene biogenic silica crash in the Andaman Sea and Bay of Bengal.

Mar. Pet. Geol. doi:10.1016/j.marpetgeo.2014.07.026

Charles, C.D., Lynch-Stieglitz, J., Ninnemann, U.S., Fairbanks, R.G., 1996. Climate connections

between the hemisphere revealed by deep sea sediment core/ice core correlations. Earth

Planet. Sci. Lett. 142, 19–27. doi:10.1016/0012-821X(96)00083-0

Cheng, H., Edwards, R.L., Broecker, W.S., Denton, G.H., Kong, X., Wang, Y., Zhang, R.,

Wang, X., 2009. Ice Age Terminations. Science 326, 248–252.

doi:10.1126/science.1177840

Clemens, S.C., Prell, W.L., 2003. A 350,000 year summer-monsoon multi-proxy stack from the
Owen Ridge, Northern Arabian Sea. Mar. Geol. 201, 35–51. doi:10.1016/S0025-
3227(03)00207-X

Clemens, S.C., Prell, W.L., 2007. The timing of orbital-scale Indian monsoon changes. Quat.
Sci. Rev. 26, 275–278. doi:10.1016/j.quascirev.2006.11.010

Clemens, S.C., Prell, W.L., Sun, Y., 2010. Orbital-scale timing and mechanisms driving Late
Pleistocene Indo-Asian summer monsoons: Reinterpreting cave speleothem δ^{18}O.
Paleoceanography 25. doi:10.1029/2010PA001926

Collett, T.S., Riedel, M., Cochran, J.R., Boswell, R., Presley, J., Kumar, P., Sathe, A., Sethi, A.,
Lall, M., Sibal, V., NGHP 01 Scientists, 2008. National Gas Hydrate Program Expedition
01 Initial Reports.

Cook, E.R., Anchukaitis, K.J., Buckley, B.M., D'Arrigo, R.D., Jacoby, G.C., Wright, W.E.,
2010. Asian Monsoon Failure and Megadrought During the Last Millennium. Science
328, 486–489. doi:10.1126/science.1185188

Crowley, T.J., 1995. Ice Age terrestrial carbon changes revisited. Glob. Biogeochem. Cycles 9,
377–389. doi:10.1029/95GB01107

Curry, W.B., Oppo, D.W., 2005. Glacial water mass geometry and the distribution of δ 13C of
ΣCO2 in the western Atlantic Ocean: Glacial Water Mass Geometry. Paleoceanography
20. doi:10.1029/2004PA001021

Davis, R.E., 1976. Predictability of Sea Surface Temperature and Sea Level Pressure Anomalies
over the North Pacific Ocean. J. Phys. Oceanogr. 6, 249–266. doi:10.1175/1520-
0485(1976)006<0249:POSSTA>2.0.CO;2

Dekens, P.S., Lea, D.W., Pak, D.K., Spero, H.J., 2002. Core top calibration of Mg/Ca in tropical foraminifera: Refining paleotemperature estimation: CORE TOP CALIBRATION. Geochem. Geophys. Geosystems 3, 1–29. doi:10.1029/2001GC000200

Deplazes, G., Lückge, A., Peterson, L.C., Timmermann, A., Hamann, Y., Hughen, K.A., Röhl, U., Laj, C., Cane, M.A., Sigman, D.M., Haug, G.H., 2013. Links between tropical rainfall and North Atlantic climate during the last glacial period. Nat. Geosci. 6, 213–217. doi:10.1038/ngeo1712

Duplessy, J.C., Shackleton, N.J., Fairbanks, R.G., Labeyrie, L., Oppo, D., Kallel, N., 1988. Deepwater source variations during the last climatic cycle and their impact on the global deepwater circulation. Paleoceanography 3, 343–360. doi:10.1029/PA003i003p00343

Epstein, S., Buchsbaum, R., Lowenstam, H.A., Urey, H.C., 1953. REVISED CARBONATE-WATER ISOTOPIC TEMPERATURE SCALE. Geol. Soc. Am. Bull. 64, 1315. doi:10.1130/0016-7606(1953)64[1315:RCITS]2.0.CO;2

Govil, P., Naidu, P.D., 2011. Variations of Indian monsoon precipitation during the last 32kyr reflected in the surface hydrography of the Western Bay of Bengal. Quat. Sci. Rev. 30, 3871–3879. doi:10.1016/j.quascirev.2011.10.004

Greenland Ice-core Project (GRIP) Members, 1993. Climate instability during the last interglacial period recorded in the GRIP ice core. Nature 364, 203–207. doi:10.1038/364203a0

Grootes, P.M., Stuiver, M., White, J.W.C., Johnsen, S., Jouzel, J., 1993. Comparison of oxygen isotope records from the GISP2 and GRIP Greenland ice cores. Nature 366, 552–554. doi:10.1038/366552a0

Guptha, M.V.S., Curry, W.B., Ittlekkot, V., Muralinath, A.S., 1997. Seasonal variation in the
flux of planktic foraminifera: sediment trap results from the Bay of Bengal, Northern
Indian Ocean. J. Foraminifer. Res. 27, 5–19.

Hendry, K.R., Robinson, L.F., Meredith, M.P., Mulitza, S., Chiessi, C.M., Arz, H., 2012. Abrupt
changes in high-latitude nutrient supply to the Atlantic during the last glacial cycle.
Geology 40, 123–126. doi:10.1130/G32779.1

Johnson, K.R., 2011. Palaeoclimate: Long-distance relationship. Nat. Geosci. 4, 426–427.
doi:10.1038/ngeo1190

Jung, S.J.A., Kroon, D., 2011. Quantifying rates of change in ocean conditions with implications
for timing of sea level change. Glob. Planet. Change 79, 204–213.
doi:10.1016/j.gloplacha.2010.11.004

Jung, S.J.A., Kroon, D., Ganssen, G., Peeters, F., Ganeshram, R., 2009. Enhanced Arabian Sea
intermediate water flow during glacial North Atlantic cold phases. Earth Planet. Sci. Lett.
280, 220–228. doi:10.1016/j.epsl.2009.01.037

Kallel, N., Labeyrie, L.D., Juillet-Leclerc, A., Duplessy, J.-C., 1988. A deep hydrological front
between intermediate and deep-wafpr , masses in the glacial Indian Ocean. Nature 333,
651–655. doi:10.1038/333651a0

Kim, S.-T., O'Neil, J.R., 1997. Equilibrium and nonequilibrium oxygen isotope effects in
synthetic carbonates. Geochim. Cosmochim. Acta 61, 3461–3475. doi:10.1016/S0016-
7037(97)00169-5

Kroopnick, P.M., 1985. The distribution of 13C of ΣCO2 in the world oceans. Deep Sea Res.
Part Oceanogr. Res. Pap. 32, 57–84. doi:10.1016/0198-0149(85)90017-2

Kudrass, H.R., Hofmann, A., Doose, H., Emeis, K., Erlenkeuser, H., 2001. Modulation and
amplification of climatic changes in the Northern Hemisphere by the Indian summer
monsoon during the past 80 k.y. Geology 29, 63. doi:10.1130/0091-
7613(2001)029<0063:MAAOCC>2.0.CO;2

Lisiecki, L.E., Raymo, M.E., 2005. A Pliocene-Pleistocene stack of 57 globally distributed
benthic δ 18O records: PLIOCENE-PLEISTOCENE BENTHIC STACK.
Paleoceanography 20, n/a–n/a. doi:10.1029/2004PA001071

Lynch-Stieglitz, J., Fairbanks, R.G., Charles, C.D., 1994. Glacial-interglacial history of Antarctic
Intermediate Water: Relative strengths of Antarctic versus Indian Ocean sources.
Paleoceanography 9, 7–29. doi:10.1029/93PA02446

Lynch-Stieglitz, J., van Geen, A., Fairbanks, R.G., 1996. Interocean exchange of glacial North
Atlantic Intermediate Water: Evidence from subantarctic Cd/Ca and carbon isotope
measurements. Paleoceanography 11, 191–201. doi:10.1029/95PA03772

Mackensen, A., Hubberten, H.-W., Bickert, T., Fischer, G., Fütterer, D.K., 1993. The δ 13C in
benthic foraminiferal tests of Fontbotia wuellerstorfi (Schwager) Relative to the δ 13C of
dissolved inorganic carbon in Southern Ocean Deep Water: Implications for glacial ocean
circulation models. Paleoceanography 8, 587–610. doi:10.1029/93PA01291

Makou, M.C., Oppo, D.W., Curry, W.B., 2010. South Atlantic intermediate water mass
geometry for the last glacial maximum from foraminiferal Cd/Ca. Paleoceanography 25.
doi:10.1029/2010PA001962

Malaizé, B., Joly, C., Vénec-Peyré, M.-T., Bassinot, F., Caillon, N., Charlier, K., 2006. Phase lag
between Intertropical Convergence Zone migration and subtropical monsoon onset over
the northwestern Indian Ocean during Marine Isotopic Substage 6.5 (MIS 6.5): ITCZ

MIGRATION AND MONSOON ONSET. Geochem. Geophys. Geosystems 7, n/a–n/a. doi:10.1029/2006GC001353

Malik, N., Bookhagen, B., Marwan, N., Kurths, J., 2012. Analysis of spatial and temporal extreme monsoonal rainfall over South Asia using complex networks. Clim. Dyn. 39, 971–987. doi:10.1007/s00382-011-1156-4

Marchitto, T.M., Broecker, W.S., 2006. Deep water mass geometry in the glacial Atlantic Ocean: A review of constraints from the paleonutrient proxy Cd/Ca: DEEP WATER MASS GEOMETRY. Geochem. Geophys. Geosystems 7. doi:10.1029/2006GC001323

Marzin, C., Kallel, N., Kageyama, M., Duplessy, J.-C., Braconnot, P., 2013. Glacial fluctuations of the Indian monsoon and their relationship with North Atlantic climate: new data and modelling experiments. Clim. Past 9, 2135–2151. doi:10.5194/cp-9-2135-2013

Mohtadi, M., Prange, M., Oppo, D.W., De Pol-Holz, R., Merkel, U., Zhang, X., Steinke, S., Lückge, A., 2014. North Atlantic forcing of tropical Indian Ocean climate. Nature 509, 76–80. doi:10.1038/nature13196

Morley, J.J., Heusser, L.E., 1997. Role of orbital forcing in east Asian monsoon climates during the last 350 kyr: Evidence from terrestrial and marine climate proxies from core RC14-99. Paleoceanography 12, 483–493. doi:10.1029/97PA00213

Mulitza, S., Boltovskoy, D., Donner, B., Meggers, H., Paul, A., Wefer, G., 2003. Temperature:δ18O relationships of planktonic foraminifera collected from surface waters. Palaeogeogr. Palaeoclimatol. Palaeoecol. 202, 143–152. doi:10.1016/S0031-0182(03)00633-3

Naqvi, W.A., Charles, C.D., Fairbanks, R.G., 1994. Carbon and oxygen isotopic records of benthic foraminifera from the Northeast Indian Ocean: implications on glacial-

interglacial atmospheric CO2 changes. Earth Planet. Sci. Lett. 121, 99–110. doi:10.1016/0012-821X(94)90034-5

Olson, D.B., Hitchcock, G.L., Fine, R.A., Warren, B.A., 1993. Maintenance of the low-oxygen layer in the central Arabian Sea. Deep Sea Res. Part II Top. Stud. Oceanogr. 40, 673–685. doi:10.1016/0967-0645(93)90051-N

Oppo, D.W., Horowitz, M., 2000. Glacial deep water geometry: South Atlantic benthic foraminiferal Cd/Ca and δ 13C evidence. Paleoceanography 15, 147–160. doi:10.1029/1999PA000436

Oppo, D.W., Lehman, S.J., 1993. Mid-Depth Circulation of the Subpolar North Atlantic During the Last Glacial Maximum. Science 259, 1148–1152. doi:10.1126/science.259.5098.1148

Pahnke, K., Goldstein, S.L., Hemming, S.R., 2008. Abrupt changes in Antarctic Intermediate Water circulation over the past 25,000 years. Nat. Geosci. 1, 870–874. doi:10.1038/ngeo360

Pahnke, K., Zahn, R., 2005. Southern Hemisphere Water Mass Conversion Linked with North Atlantic Climate Variability. Science 307, 1741–1746. doi:10.1126/science.1102163

Phillips, S., Johnson, J., Giosan, L., Rose, K., 2014. Monsoon-influenced variation in productivity and lithogenic sediment flux since 110 ka in the Mahanadi Basin, offshore India.

Pichevin, L., Bard, E., Martinez, P., Billy, I., 2007. Evidence of ventilation changes in the Arabian Sea during the late Quaternary: Implication for denitrification and nitrous oxide emission: VENTILATION CHANGES IN THE ARABIAN SEA. Glob. Biogeochem. Cycles 21, n/a–n/a. doi:10.1029/2006GB002852

Prasanna Kumar, S., Muraleedharan, P.M., Prasad, T.G., Gauns, M., Ramaiah, N., de Souza, S.N., Sardesai, S., Madhupratap, M., 2002. Why is the Bay of Bengal less productive during summer monsoon compared to the Arabian Sea? Geophys. Res. Lett. 29. doi:10.1029/2002GL016013

Railsback, L.B., Anderson, T.F., Ackerly, S.C., Cisne, J.L., 1989. Paleoceanographic modeling of temperature-salinity profiles from stable isotopic data. Paleoceanography 4, 585–591. doi:10.1029/PA004i005p00585

Rashid, H., England, E., Thompson, L., Polyak, L., 2011. Late Glacial to Holocene Indian Summer Monsoon Variability Based upon Sediment Records Taken from the Bay of Bengal. Terr. Atmospheric Ocean. Sci. 22, 215. doi:10.3319/TAO.2010.09.17.02(TibXS)

Rashid, H., Flower, B.P., Poore, R.Z., Quinn, T.M., 2007. A ~25ka Indian Ocean monsoon variability record from the Andaman Sea. Quat. Sci. Rev. 26, 2586–2597. doi:10.1016/j.quascirev.2007.07.002

Raza, T., Ahmad, S.M., Sahoo, M., Banerjee, B., Bal, I., Dash, S., Suseela, G., Mukherjee, I., 2014. Hydrographic changes in the southern Bay of Bengal during the last ~65,000 y inferred from carbon and oxygen isotopes of foraminiferal fossil shells. Quat. Int. 333, 77–85. doi:10.1016/j.quaint.2014.02.010

Rickaby, R.E.M., Elderfield, H., 2005. Evidence from the high-latitude North Atlantic for variations in Antarctic Intermediate water flow during the last deglaciation. Geochem. Geophys. Geosystems 6, n/a–n/a. doi:10.1029/2004GC000858

Rohling, E.J., Bigg, G.R., 1998. Paleosalinity and δ 18O: A critical assessment. J. Geophys. Res. 103, 1307. doi:10.1029/97JC01047

Rohling, E.J., Liu, Q.S., Roberts, A.P., Stanford, J.D., Rasmussen, S.O., Langen, P.L., Siddall, M., 2009. Controls on the East Asian monsoon during the last glacial cycle, based on comparison between Hulu Cave and polar ice-core records. Quat. Sci. Rev. 28, 3291–3302. doi:10.1016/j.quascirev.2009.09.007

Rosenthal, Y., Field, M.P., Sherrell, R.M., 1999. Precise Determination of Element/Calcium Ratios in Calcareous Samples Using Sector Field Inductively Coupled Plasma Mass Spectrometry. Anal. Chem. 71, 3248–3253. doi:10.1021/ac981410x

Ruddiman, W.F., 2001. Earth's climate: past and future. W.H. Freeman, New York.

Ruddiman, W.F., 2006. What is the timing of orbital-scale monsoon changes? Quat. Sci. Rev. 25, 657–658. doi:10.1016/j.quascirev.2006.02.004

Sarma, V.V.S.S., 2002. An evaluation of physical and biogeochemical processes regulating perennial suboxic conditions in the water column of the Arabian Sea: PERENNIAL EXISTENCE OF SUBOXIC ZONE IN THE ARABIAN SEA. Glob. Biogeochem. Cycles 16, 29–1–29–11. doi:10.1029/2001GB001461

Sarmiento, J.L., Gruber, N., Brzezinski, M.A., Dunne, J.P., 2004. High-latitude controls of thermocline nutrients and low latitude biological productivity. Nature 427, 56–60. doi:10.1038/nature02127

Schlitzer, R., 2014. eGEOTRACES - Electronic Atlas of GEOTRACES Sections and Animated 3D Scenes [WWW Document]. URL http://www.egeotraces.org

Schmittner, A., Galbraith, E.D., Hostetler, S.W., Pedersen, T.F., Zhang, R., 2007. Large fluctuations of dissolved oxygen in the Indian and Pacific oceans during Dansgaard-Oeschger oscillations caused by variations of North Atlantic Deep Water subduction:

OXYGEN DURING D/O OSCILLATIONS. Paleoceanography 22, n/a–n/a.
doi:10.1029/2006PA001384

Schulenberg, S., 2011. Reconstructing The Variability In The Indian Monsoon From The Last
Glacial Period To Present. University of New Hampshire.

Schulz, H., von Rad, U., Erlenkeuser, H., 1998. Correlation between Arabian Sea and Greenland
climate oscillations of the past 110,000 years. Nature 393, 54–57.

Shackleton, N.J., Hall, M.A., Vincent, E., 2000. Phase relationships between millennial-scale
events 64,000-24,000 years ago. Paleoceanography 15, 565–569.
doi:10.1029/2000PA000513

Siddall, M., Rohling, E.J., Almogi-Labin, A., Hemleben, C., Meischner, D., Schmelzer, I.,
Smeed, D.A., 2003. Sea-level fluctuations during the last glacial cycle. Nature 423, 853–
858. doi:10.1038/nature01690

Slowey, N.C., Curry, W.B., 1995. Glacial-interglacial differences in circulation and carbon
cycling within the upper western North Atlantic. Paleoceanography 10, 715–732.
doi:10.1029/95PA01166

Steinke, S., Chiu, H.-Y., Yu, P.-S., Shen, C.-C., Löwemark, L., Mii, H.-S., Chen, M.-T., 2005.
Mg/Ca ratios of two Globigerinoides ruber (white) morphotypes: Implications for
reconstructing past tropical/subtropical surface water conditions: G. RUBER (WHITE)
MG/CA RATIOS. Geochem. Geophys. Geosystems 6, n/a–n/a.
doi:10.1029/2005GC000926

Stuvier, M., Reimer, P.J., 1993. Extended C-14 Data-Base And Revised Calib 3.0 C-14 Age
Calibration Program. RADIOCARBON 35, 215–230.

Talley, L.D., Pickard, G.L., Emery, W.J. (Eds.), 2011. Descriptive physical oceanography: an introduction, 6th ed. ed. Academic Press, Amsterdam ; Boston.

Tomczak, M., Godfrey, J.S., 2003. Regional oceanography: an Introduction. Daya, Delhi.

Wang, Y.J., Cheng, H., Edwards, R.L., An, Z., Wu, J., Shen, C.-C., Dorale, J.A., 2001. A High-Resolution Absolute-Dated Late Pleistocene Monsoon Record from Hulu Cave, China. Science 294, 2345–2348. doi:10.1126/science.1064618

Woods Hole Oceanographic Institution, 2012. Instruments: Plasma Mass Spectrometry Facility [WWW Document]. URL http://www.whoi.edu/page.do?pid=31617

You, Y., 1998. Intermediate water circulation and ventilation of the Indian Ocean derived from water-mass contributions. J. Mar. Res. 56, 1029–1067. doi:10.1357/002224098765173455

Yuan, D., Cheng, H., Edwards, R.L., Dykoski, C.A., Kelly, M.J., Zhang, M., Qing, J., Lin, Y., Wu, J., Dorale, J.A., An, Z., Cai, Y., 2004. Timing, Duration, and Transitions of the Last Interglacial Asian Monsoon. Science 304, 575–578. doi:10.1126/science.1091220

Ziegler, M., Lourens, L.J., Tuenter, E., Hilgen, F., Reichart, G.-J., Weber, N., 2010. Precession phasing offset between Indian summer monsoon and Arabian Sea productivity linked to changes in Atlantic overturning circulation. Paleoceanography 25. doi:10.1029/2009PA001884

Appendix (Tables)

Table 1: Radiocarbon Dates for Core 19 B.

Core	Depth (cm)	Adjusted Depth (cmbsf)	Species	Calib 7.0 MARINE 13 date (BP) 1, 2σ lower upper	Mean Age (BP)
NGHP-01--19A-1H-3	20-22	324.8	mixed planktonic	19492 19731 19376 19899	19610
NOSAMS data:		**Number** OS-66068	**Radiocarbon Age** 16,650	**AMS error** 80	Schulenburg et al. 2011
NGHP-01--19A-1H-3	54-55	354.5	*G. ruber*	26648 26995 26504 27159	26820
NOSAMS data:		OS-89468	22,900	80	Schulenburg et al. 2011
NGHP-01--19A-1H-3	91-93	395.8	mixed planktonic	31053 31241 30957 31338	31150
NOSAMS data:		OS-66069	27,600	120	Phillips et al. 2014
NGHP-01--19B-1H-3	142-143	442.5	*G. sacculifer*	38208 38658 37789 38845	38430
NOSAMS data:		OS-109301	34,300	200	this study
NGHP-01--19A-1H-3	64-65	514.5	*G. sacculifer*	41896 42561 41524 42894	42230
NOSAMS data:		OS-109452	38,400	500	this study
NGHP-01--19B-1H-4	136-137	586.5	*G. sacculifer*	N/A	-
NOSAMS data:		OS-109561	50,600	7,500	this study
NGHP-01--19A-2H-1	84-86	618.8	mixed planktonic	N/A	-
NOSAMS data:		OS-66070	48,000	650	Phillips et al. 2014

Table 2: Sedimentation Rates for Core 19 B.

Depth (cmbsf)	Method	Age (BP)	Sedimentation Rate (cm/kyr)
324.8	^{14}C	19610	
354.5	^{14}C	26820	4.1
395.8	^{14}C	31150	9.5
442.5	^{14}C	38430	6.4
610.5	benthic ^{18}O	55000	10.1

Table 3. Quadratic Best Fit Equations. Used to generate residuals and averages for trends.

Variable	Quadratic Fit Equation
SST	$= 1.0E\text{-}9(age)^2 - 1.1E\text{-}4(age) + 28.0$
$\delta^{18}O_{sw}$	$= 1.7E\text{-}9(age)^2 - 1.5E\text{-}4(age) + 4.28$
$\delta^{13}C_{pl}$	$= -6.4E\text{-}10(age)^2 + 3.6E\text{-}05(age) + 0.25$
$\delta^{18}O_{ben}$	$= -3.7E\text{-}10(age)^2 + 1.8E\text{-}5(age) + 3.31$
$\delta^{13}C_{ben}$	$= -3.7E\text{-}10(age)^2 + 1.5E\text{-}5(age) - 0.27$

Table 4: Planktic Stable Isotope Data. All data was measured in approximately 60-70 μg samples of *G. ruber* white, s.s. morphotype, 212-250 μm size fraction. Samples are either from picks of around 10 individual specimens, or were an aliquot of a 50 specimen sample which was homogenized with the trace element samples. Raw data shown along with $\delta^{18}O_{sw}$ (temperature-corrected).

Core	Depth cm	MCD cmbsf	Age years BP	Description	$\delta^{13}C_c$ PDB; ‰	$\delta^{18}O_c$ PBD; ‰	$\delta^{18}O_{sw}$ SMOW; ‰
NGHP-01--19B-1H-3	42-43	342.5	23907	Homogenized with trace element sample (50)	0.72	-1.05	1.65
NGHP-01--19B-1H-3	42-43	342.5	23907	Homogenized with trace element sample (50)	0.46	-0.99	1.72
NGHP-01--19B-1H-3	46-47	346.5	24878	Homogenized with trace element sample (50)	0.74	-1.14	1.23
NGHP-01--19B-1H-3	46-47	346.5	24878	10 specimens	1.07	-1.12	1.25
NGHP-01--19B-1H-3	46-47	346.5	24878	10 specimens	0.82	-1.04	1.33
NGHP-01--19B-1H-3	51-52	351.5	26092	Homogenized with trace element sample (50)	0.69	-1.08	1.45
NGHP-01--19B-1H-3	51-52	351.5	26092	Homogenized with trace element sample (50)	0.71	-1.10	1.43
NGHP-01--19B-1H-3	54-55	354.5	26820	Homogenized with trace element sample (50)	1.03	-1.51	1.21
NGHP-01--19B-1H-3	54-55	354.5	26820	10 specimens	0.97	-1.29	1.44
NGHP-01--19B-1H-3	54-55	354.5	26820	10 specimens	0.76	-1.18	1.55
NGHP-01--19B-1H-3	66-67	366.5	28078	Homogenized with trace element sample (44)	0.83	-1.22	1.36
NGHP-01--19B-1H-3	74-75	374.5	28917	Homogenized with trace element sample (50)	0.50	-1.13	1.31

Table 4 continued

Core	Depth cm	MCD cmbsf	Age years BP	Description	$\delta^{13}C_c$ PDB; ‰	$\delta^{18}O_c$ PBD; ‰	$\delta^{18}O_{sw}$ SMOW; ‰
NGHP-01--19B-1H-3	77-78	377.5	29231	Homogenized with trace element sample (45)	0.88	-1.50	1.00
NGHP-01--19B-1H-3	81-82	381.5	29651	Homogenized with trace element sample (50)	0.61	-1.39	1.16
NGHP-01--19B-1H-3	86-87	386.5	30175	10 specimens	0.75	-1.48	1.06
NGHP-01--19B-1H-3	90-91	390.5	30594	Homogenized with trace element sample (50)	0.83	-1.27	1.73
NGHP-01--19B-1H-3	94-95	394.5	31014	11 specimens	0.70	-1.29	1.38
NGHP-01--19B-1H-3	98-99	398.5	31571	Homogenized with trace element sample (50)	0.97	-1.55	0.95
NGHP-01--19B-1H-3	98-99	398.5	31571	Homogenized with trace element sample (50)	0.78	-1.45	1.06
NGHP-01--19B-1H-3	102-103	402.5	32194	10 specimens	0.87	-1.42	1.15
NGHP-01--19B-1H-3	107-108	407.5	32974	Homogenized with trace element sample (50)	0.45	-1.33	0.99
NGHP-01--19B-1H-3	107-108	407.5	32974	Homogenized with trace element sample (50)	0.75	-1.32	1.00
NGHP-01--19B-1H-3	110-111	410.5	33442	10 specimens	0.73	-0.99	1.39
NGHP-01--19B-1H-3	114-115	414.5	34065	10 specimens	0.38	-1.41	0.93
NGHP-01--19B-1H-3	118-119	418.5	34689	10 specimens	0.38	-1.08	1.18
NGHP-01--19B-1H-3	122-123	422.5	35312	Homogenized with trace element sample (50)	0.86	-1.56	0.95
NGHP-01--19B-1H-3	126-127	426.5	35936	8 specimens	-0.06 (outlier)	-1.56	1.17
NGHP-01--19B-1H-3	130-131	430.5	36559	10 specimens	0.99	-1.23	1.41
NGHP-01--19B-1H-3	135-136	435.5	37339	9 specimens	0.73	-1.58	1.04
NGHP-01--19B-1H-3	138-139	438.5	37806	Homogenized with trace element sample (50)	0.69	-1.43	1.13
NGHP-01--19B-1H-3	142-142	442.5	38430	10 specimens	0.60	-1.38	1.25

Table 4 continued

Core	Depth cm	MCD cmbsf	Age years BP	Description	$\delta^{13}C_c$ PDB; ‰	$\delta^{18}O_c$ PBD; ‰	$\delta^{18}O_{sw}$ SMOW; ‰
NGHP-01--19B-1H-3	146-147	446.5	38825	Homogenized with trace element sample (50)	0.45	-1.34	1.17
NGHP-01--19B-1H-4	1-2	450.5	39219	10 specimens	0.83	-1.65	1.32
NGHP-01--19B-1H-4	4-5	454.5	39614	Homogenized with trace element sample (50)	0.88	-1.30	0.88
NGHP-01--19B-1H-4	8-9	458.5	40008	10 specimens	0.52	-0.84 (outlier)	-
NGHP-01--19B-1H-4	10-11	460.5	40205	Homogenized with trace element sample (50)	0.91	-1.66	0.87
NGHP-01--19B-1H-4	16-17	466.5	40797	10 specimens	0.69	-1.33	0.87
NGHP-01--19B-1H-4	20-21	470.5	41192	10 specimens	0.50	-1.46	1.01
NGHP-01--19B-1H-4	25-26	475.5	41685	Homogenized with trace element sample (50)	0.70	-1.52	0.82
NGHP-01--19B-1H-4	28-29	478.5	41981	Homogenized with trace element sample (50)	0.90	-1.62	0.54
NGHP-01--19B-1H-4	32-33	482.5	42375	Homogenized with trace element sample (50)	0.83	-1.80	0.60
NGHP-01--19B-1H-4	39-40	489.5	43066	Homogenized with trace element sample (50)	0.46	-1.85	0.73
NGHP-01--19B-1H-4	44-45	494.5	43559	Homogenized with trace element sample (50)	0.46	-1.57	0.92
NGHP-01--19B-1H-4	48-49	498.5	43953	Homogenized with trace element sample (50)	0.53	-1.65	0.82
NGHP-01--19B-1H-4	53-54	503.5	44446	Homogenized with trace element sample (50)	0.52	-1.47	0.98
NGHP-01--19B-1H-4	56-57	506.5	44742	Homogenized with trace element sample (50)	0.38	-1.33	1.14
NGHP-01--19B-1H-4	60-61	510.5	45137	Homogenized with trace element sample (50)	0.24	-1.47	0.80
NGHP-01--19B-1H-4	64-65	514.5	45531	Homogenized with trace element sample (50)	0.54	-1.78	0.58
NGHP-01--19B-1H-4	64-65	514.5	45531	Homogenized with trace element sample (50)	0.77	-1.59	0.77
NGHP-01--19B-1H-4	67-68	517.5	45827	Homogenized with trace element sample (50)	0.61	-1.65	0.71

Table 4 continued

Core	Depth cm	MCD cmbsf	Age years BP	Description	$\delta^{13}C_c$ PDB; ‰	$\delta^{18}O_c$ PBD; ‰	$\delta^{18}O_{sw}$ SMOW; ‰
NGHP-01--19B-1H-4	70-71	520.5	46123	Homogenized with trace element sample (50)	0.63	-1.95	0.48
NGHP-01--19B-1H-4	72-73	522.5	46320	Homogenized with trace element sample (50)	0.48	-1.62	0.81
NGHP-01--19B-1H-4	76-77	526.5	46715	Homogenized with trace element sample (50)	0.66	-1.62	0.67
NGHP-01--19B-1H-4	81-82	531.5	47208	Homogenized with trace element sample (50)	0.85	-1.60	0.55
NGHP-01--19B-1H-4	81-82	531.5	47208	Homogenized with trace element sample (50)	0.59	-1.73	0.42
NGHP-01--19B-1H-4	84-85	534.5	47504	Homogenized with trace element sample (50)	0.40	-1.38	0.94
NGHP-01--19B-1H-4	88-89	538.5	47899	10 specimens	0.70	-1.63	0.85
NGHP-01--19B-1H-4	96-97	546.5	48688	Homogenized with trace element sample (50)	0.66	-2.00	0.46
NGHP-01--19B-1H-4	99-100	549.5	48984	Homogenized with trace element sample (50)	0.59	-1.42	1.04
NGHP-01--19B-1H-4	104-105	554.5	49477	Homogenized with trace element sample (50)	0.62	-1.63	0.81
NGHP-01--19B-1H-4	109-110	559.5	49970	Homogenized with trace element sample (50)	0.50	-1.50	0.95
NGHP-01--19B-1H-4	112-113	562.5	50266	10 specimens	0.73	-1.69	0.75
NGHP-01--19B-1H-4	120-121	570.5	51055	10 specimens	0.52	-1.59	0.86
NGHP-01--19B-1H-4	124-125	574.5	51449	Homogenized with trace element sample (45)	0.51	-1.48	0.96
NGHP-01--19B-1H-4	128-129	578.5	51844	Homogenized with trace element sample (50)	0.49	-1.61	0.83
NGHP-01--19B-1H-4	130-131	580.5	52041	Homogenized with trace element sample (50)	0.23	-1.67	0.78
NGHP-01--19B-1H-4	130-131	580.5	52041	Homogenized with trace element sample (50)	0.26	-1.70	0.74
NGHP-01--19B-1H-4	133-134	583.5	52337	Homogenized with trace element sample (50)	0.42	-1.69	0.74
NGHP-01--19B-1H-4	136-137	586.5	52633	Homogenized with trace element sample (50)	0.35	-1.62	0.89

Table 4 continued

Core	Depth cm	MCD cmbsf	Age years BP	Description	$\delta^{13}C_c$ PDB; ‰	$\delta^{18}O_c$ PBD; ‰	$\delta^{18}O_{sw}$ SMOW; ‰
NGHP-01--19B-1H-4	140-141	590.5	53027	Homogenized with trace element sample (50)	0.23	-1.48	1.10
NGHP-01--19B-1H-4	144-145	594.5	53422	Homogenized with trace element sample (50)	0.18	-1.28	1.30
NGHP-01--19B-1H-4	148-end	598.5	53816	Homogenized with trace element sample (50)	0.36	-1.34	1.24
NGHP-01--19B-1H-5	2-3	602.5	54211	Homogenized with trace element sample (50)	-0.12	-1.47	1.11
NGHP-01--19B-1H-5	6-7	606.5	54605	Homogenized with trace element sample (50)	0.53	-1.28	1.30
NGHP-01--19B-1H-5	10-11	610.0	54951	Homogenized with trace element sample (50)	0.44	-1.39	1.19
NGHP-01--19B-1H-5	10-11	611.0	55049	Homogenized with trace element sample (50)	0.48	-1.26	1.32

Table 5: Planktic Trace Element Data. All measured in approximately 140 μg samples from 40-50 specimens of *G. ruber* white, s.s. morphotype, 212-250 μm size fraction.

Core	Depth cm	MCD cmbsf	Age yrs BP	Mg/Ca mmol mol^{-1}	Near Surface Temperature °C
NGHP-01--19B-1H-3	42-43	342.5	23907	4.06	26.31
NGHP-01--19B-1H-3	42-43	342.5	23907	3.98	26.09
NGHP-01--19B-1H-3	46-47	346.5	24878	3.52	24.73
NGHP-01--19B-1H-3	51-52	351.5	26092	3.63	25.08
NGHP-01--19B-1H-3	51-52	351.5	26092	3.86	25.77
NGHP-01--19B-1H-3	54-55	354.5	26820	4.05	26.30
NGHP-01--19B-1H-3	74-75	374.5	28917	3.61	25.03
NGHP-01--19B-1H-3	81-82	381.5	29651	3.78	25.54
NGHP-01--19B-1H-3	86-87	386.5	30175	3.77	25.50

Table 5 continued

Core	Depth cm	MCD cmbsf	Age yrs BP	Mg/Ca mmol mol^{-1}	Near Surface Temperature °C
NGHP-01--19B-1H-3	86-87	386.5	30175	3.77	25.50
NGHP-01--19B-1H-3	90-91	390.5	30594	4.53	27.54
NGHP-01--19B-1H-3	94-95	394.5	31014	3.95	26.03
NGHP-01--19B-1H-3	98-99	398.5	31571	3.71	25.33
NGHP-01--19B-1H-3	102-103	402.5	32194	3.82	25.64
NGHP-01--19B-1H-3	107-108	407.5	32974	3.26	23.88
NGHP-01--19B-1H-3	107-108	407.5	32974	3.64	25.12
NGHP-01--19B-1H-3	110-111	410.5	33442	3.52	24.74
NGHP-01--19B-1H-3	114-115	414.5	34065	3.48	24.62
NGHP-01--19B-1H-3	118-119	418.5	34689	3.36	24.23
NGHP-01--19B-1H-3	122-123	422.5	35312	3.72	25.34
NGHP-01--19B-1H-3	126-127	426.5	35936	4.07	26.34
NGHP-01--19B-1H-3	130-131	430.5	36559	3.92	25.93
NGHP-01--19B-1H-3	135-136	435.5	37339	3.87	25.79
NGHP-01--19B-1H-3	138-139	438.5	37806	3.70	25.28
NGHP-01--19B-1H-3	142-142	442.5	38430	3.91	25.89
NGHP-01--19B-1H-3	146-147	446.5	38825	3.66	25.18
NGHP-01--19B-1H-3	146-147	446.5	38825	3.79	25.55
NGHP-01--19B-1H-4	0-1	450.5	39219	4.47	27.39
NGHP-01--19B-1H-4	4-5	454.5	39614	3.26	23.87

Table 5 continued

Core	Depth cm	MCD cmbsf	Age yrs BP	Mg/Ca mmol mol^{-1}	Near Surface Temperature °C
NGHP-01--19B-1H-4	8-9	458.5	40008	3.76	25.45
NGHP-01--19B-1H-4	16-17	466.5	40797	3.28	23.95
NGHP-01--19B-1H-4	20-21	470.5	41192	3.66	25.17
NGHP-01--19B-1H-4	25-26	475.5	41685	3.47	24.59
NGHP-01--19B-1H-4	28-29	478.5	41981	3.24	23.82
NGHP-01--19B-1H-4	32-33	482.5	42375	3.56	24.87
NGHP-01--19B-1H-4	39-40	489.5	43066	3.84	25.69
NGHP-01--19B-1H-4	44-45	494.5	43559	3.73	25.38
NGHP-01--19B-1H-4	44-45	494.5	43559	3.65	25.15
NGHP-01--19B-1H-4	48-49	498.5	43953	3.66	25.17
NGHP-01--19B-1H-4	53-54	503.5	44446	3.65	25.12
NGHP-01--19B-1H-4	53-54	503.5	44446	3.62	25.04
NGHP-01--19B-1H-4	56-57	506.5	44742	3.66	25.17
NGHP-01--19B-1H-4	60-61	510.5	45137	3.32	24.08
NGHP-01--19B-1H-4	60-61	510.5	45137	3.46	24.53
NGHP-01--19B-1H-4	64-65	514.5	45531	3.6	24.97
NGHP-01--19B-1H-4	64-65	514.5	45531	3.41	24.38
NGHP-01--19B-1H-4	72-73	522.5	46320	3.6	24.97
NGHP-01--19B-1H-4	81-82	531.5	47208	3.22	23.73

Table 5 continued

Core	Depth cm	MCD cmbsf	Age yrs BP	Mg/Ca mmol mol^{-1}	Near Surface Temperature °C
NGHP-01--19B-1H-4	92-93	542.5	48293	3.67	25.21
NGHP-01--19B-1H-4	99-100	549.5	48984	3.65	25.12
NGHP-01--19B-1H-4	133-134	583.5	52337	3.6	24.98
NGHP-01--19B-1H-4	140-141	590.5	53027	3.83	25.66

Table 6: Benthic Stable Isotope Data. All samples are of the genus *Cibicidoides*, picked from all size fractions >212 μm; samples ranged from 100 to 200 μg.

Core	Depth cm	MCD cmbsf	Age yrs BP	Description	δ^{13}C PDB; ‰	δ^{18}O PBD; ‰
NGHP-01--19B-1H-3	30-31	330.5	20994	5 C. pachyderma	-0.21	3.37
NGHP-01--19B-1H-3	38-39	338.5	22936	6 C. pachyderma	-0.19	3.69
NGHP-01--19B-1H-3	42-43	342.5	23907	4 C. pachyderma	-0.08	3.66
NGHP-01--19B-1H-3	46-47	346.5	24878	5 C. pachyderma	-0.12	3.39
NGHP-01--19B-1H-3	51-52	351.5	26092	3 C. pachyderma	-0.04	3.58
NGHP-01--19B-1H-3	62-63	362.5	27659	2 C. pachyderma + 1 C. wullerstorfi	0.06	3.45
NGHP-01--19B-1H-3	70-71	370.5	28497	2 C. pachyderma	-0.16	3.54
NGHP-01--19B-1H-3	74-75	374.5	28917	4 C. pachyderma	-0.17	3.62
NGHP-01--19B-1H-3	77-78	377.5	29231	3 C. pachyderma	-0.14	3.66
NGHP-01--19B-1H-3	81-82	381.5	29651	3 C. pachyderma	-0.13	3.52
NGHP-01--19B-1H-3	86-87	386.5	30175	3 C. pachyderma;	-0.26 (outlier)	2.35 (outlier)
NGHP-01--19B-1H-3	90-91	390.5	30594	1 C. pachyderma	-0.29	3.61
NGHP-01--19B-1H-3	94-95	394.5	31014	2 C. pachyderma + 2 C. wullerstorfi	-0.09	3.45

Table 6 continued

Core	Depth cm	MCD cmbsf	Age yrs BP	Description	$\delta^{13}C$ PDB; ‰	$\delta^{18}O$ PBD; ‰
NGHP-01--19B-1H-3	102-103	402.5	32194	2 C. pachyderma + 1 C. wullerstorfi	-0.27	3.48
NGHP-01--19B-1H-3	107-108	407.5	32974	3 C. pachyderma	-0.30	3.58
NGHP-01--19B-1H-3	107-108	410.5	33442	2 C. pachyderma	-0.36	3.39
NGHP-01--19B-1H-3	114-115	414.5	34065	1 C. pachyderma + 2 C. wullerstorfi	-0.28	3.43
NGHP-01--19B-1H-3	118-119	418.5	34689	5 C. pachyderma	-0.34	3.54
NGHP-01--19B-1H-3	122-123	422.5	35312	6 C. pachyderma	-0.34	3.41
NGHP-01--19B-1H-3	130-131	430.5	36559	3 C. pachyderma	-0.11	3.43
NGHP-01--19B-1H-3	135-136	435.5	37339	4 C. pachyderma	-0.05	3.14
NGHP-01--19B-1H-3	138-139	438.5	37806	5 C. pachyderma	-0.16	3.44
NGHP-01--19B-1H-3	142-142	442.5	38430	4 C. pachyderma	-0.16	3.40
NGHP-01--19B-1H-3	146-147	446.5	38825	6 C. pachyderma	-0.26	3.49
NGHP-01--19B-1H-4	0-1	450.5	39219	5 C. pachyderma	-0.23	3.35
NGHP-01--19B-1H-4	8-9	458.5	40008	3 C. pachyderma	-0.30	3.50
NGHP-01--19B-1H-4	10-11	460.5	40205	4 C. pachyderma	-0.17	3.39
NGHP-01--19B-1H-4	16-17	466.5	40797	5 C. pachyderma	-0.11	3.35
NGHP-01--19B-1H-4	20-21	470.5	41192	3 C. pachyderma	-0.03	3.20
NGHP-01--19B-1H-4	25-26	475.5	41685	4 C. pachyderma	-0.14	3.32
NGHP-01--19B-1H-4	28-29	478.5	41981	6 C. pachyderma	-0.39	3.53
NGHP-01--19B-1H-4	32-33	482.5	42375	5 C. pachyderma	-0.35	3.54

Table 6 continued

Core	Depth cm	MCD cmbsf	Age yrs BP	Description	$\delta^{13}C$ PDB; ‰	$\delta^{18}O$ PBD; ‰
NGHP-01--19B-1H-4	36-37	486.5	42770	5 C. pachyderma	-0.35	3.40
NGHP-01--19B-1H-4	39-40	489.5	43066	6 C. pachyderma	-0.31	3.36
NGHP-01--19B-1H-4	44-45	494.5	43559	5 C. pachyderma	-0.37	3.24
NGHP-01--19B-1H-4	48-49	498.5	43953	4 C. pachyderma	-0.06	3.06
NGHP-01--19B-1H-4	53-54	503.5	44446	4 C. pachyderma	-0.19	3.34
NGHP-01--19B-1H-4	56-57	506.5	44742	5 C. pachyderma	-0.29	3.44
NGHP-01--19B-1H-4	60-61	510.5	45137	4 C. pachyderma	-0.27	3.29
NGHP-01--19B-1H-4	64-65	514.5	45531	6 C. pachyderma	-0.30	3.43
NGHP-01--19B-1H-4	67-68	517.5	45827	6 C. pachyderma	-0.46	3.51
NGHP-01--19B-1H-4	70-71	520.5	46123	6 C. pachyderma	-0.42	3.33
NGHP-01--19B-1H-4	72-73	522.5	46320	6 C. pachyderma	-0.58	3.32
NGHP-01--19B-1H-4	76-77	526.5	46715	4 C. pachyderma	-0.44	3.58
NGHP-01--19B-1H-4	81-82	531.5	47208	5 C. pachyderma	-0.55	3.52
NGHP-01--19B-1H-4	84-85	534.5	47504	5 C. pachyderma	-0.58	3.38
NGHP-01--19B-1H-4	88-89	538.5	47899	6 C. pachyderma	-0.43	3.52
NGHP-01--19B-1H-4	92-93	542.5	48293	5 C. pachyderma	-0.49	3.40
NGHP-01--19B-1H-4	96-97	546.5	48688	4 C. pachyderma	-0.40	3.30
NGHP-01--19B-1H-4	99-100	549.5	48984	4 C. pachyderma	-0.48	3.35
NGHP-01--19B-1H-4	104-105	554.5	49477	6 C. pachyderma	-0.36	3.30

Table 6 continued

Core	Depth cm	MCD cmbsf	Age yrs BP	Description	δ¹³C PDB; ‰	δ¹⁸O PBD; ‰
NGHP-01--19B-1H-4	109-110	559.5	49970	5 C. pachyderma	-0.32	3.30
NGHP-01--19B-1H-4	112-113	562.5	50266	6 C. pachyderma	-0.60	3.42
NGHP-01--19B-1H-4	116-117	566.5	50660	6 C. pachyderma	-0.68	3.40
NGHP-01--19B-1H-4	120-121	570.5	51055	6 C. pachyderma	-0.59	3.21
NGHP-01--19B-1H-4	124-125	574.5	51449	5 C. pachyderma	-0.64	3.35
NGHP-01--19B-1H-4	128-129	578.5	51844	6 C. pachyderma	-0.69	3.20
NGHP-01--19B-1H-4	130-131	580.5	52041	6 C. pachyderma	-0.62	3.29
NGHP-01--19B-1H-4	133-134	583.5	52337	5 C. pachyderma	-0.70	3.27
NGHP-01--19B-1H-4	136-137	586.5	52633	5 C. pachyderma	-0.62	3.24
NGHP-01--19B-1H-4	140-141	590.5	53027	5 C. pachyderma	-0.69	3.32
NGHP-01--19B-1H-4	144-145	594.5	53422	5 C. pachyderma	-0.47	3.15
NGHP-01--19B-1H-4	148-end	598.5	53816	3 C. pachyderma	-0.23	2.86
NGHP-01--19B-1H-5	2-3	602.5	54211	5 C. pachyderma	-0.35	3.14
NGHP-01--19B-1H-5	6-7	606.5	54605	1 C. pachyderma	-0.13	2.83
NGHP-01--19B-1H-5	10-11	610.0	54951	4 C. pachyderma	-0.48	3.13